Recycling waste tyre polymer for production of fibre reinforced cemented tailings backfill in green mining

Guo, Zhenbang; Qiu, Jingping; Kirichek, Alex ; Zhou, Hao ; Liu, Chen; Yang, Lei

DOI
10.1016/j.scitotenv.2023.168320

Publication date
2023

Document Version
Final published version

Published in
Science of the Total Environment

Science of the Total Environment 908 (2024) 168320

Contents lists available at ScienceDirect

Science of the Total Environment

journal homepage: www.elsevier.com/locate/scitotenv

Recycling waste tyre polymer for production of fibre reinforced cemented tailings backfill in green mining

Zhenbang Guo [a,b,c], Jingping Qiu [a,b], Alex Kirichek [c], Hao Zhou [d], Chen Liu [e], Lei Yang [f,*]

[a] School of Resource and Civil Engineering, Northeastern University, Shenyang, China
[b] Science and Technology Innovation Center of Smart Water and Resource Environment, Northeastern University, Shenyang 110819, China
[c] Section of Rivers, Ports, Waterways and Dredging Engineering, Department of Hydraulic Engineering, Faculty of Civil Engineering & Geosciences, Delft University of Technology, Stevinweg 1, 2628 CN Delft, the Netherlands
[d] Xingshan Iron Mine, Mining Corporation, Shougang Group Co., Ltd., Qian'an, Hebei 064404, China
[e] Department of Materials and Environment (Microlab), Faculty of Civil Engineering and Geoscience, Delft University of Technology, Delft, the Netherlands
[f] Hopkins Extreme Materials Institute, Johns Hopkins University, Baltimore, MD 21218, USA

HIGHLIGHTS

- WFT and fibre flocculation jointly control the dynamic yield stress.
- The mechanical properties of CTB increase first and then drop with RTPF content.
- For a given RTPF content, the optimal viscosity is constant.
- The application of RTPF in CTB has greater advantages compared with PPF.

GRAPHICAL ABSTRACT

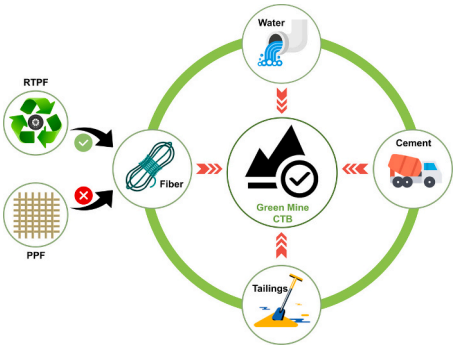

ARTICLE INFO

Editor: Daniel CW Tsang

Keywords:
Solid waste utilization
Recycled Tyre polymer fibre
Cemented tailings backfill
Rheology
Strength
Microstructure

ABSTRACT

The increasing amount of solid waste, e.g., waste tyres from car industry and tailings from mine operations, causes substantial environmental and societal issues. The recycled tyre polymer fibre (RTPF) reinforced cemented tailings backfill (CTB) is a kind of composite that can treat waste tyres and tailings simultaneously and realize green mining, but its engineering properties have not been well understood. In this study, the rheology (i.e., static and dynamic yield stress, and structural build-up), strength (i.e., uniaxial and triaxial compressive, splitting tensile and flexural strengths), microstructure, and life cycle of RTPF reinforced CTB are comprehensively evaluated. For comparison, the engineering performance of the commonly used polypropylene fibre (PPF) reinforced CTB in mines is tested. The experimental results demonstrate that incorporating 0.6 wt% RTPF into CTB can achieve comparable fluidity and strength to the CTB reinforced with 0.3 wt% PPF at reduced cost and improved sustainability. A strength enhancement approach for RTPF reinforced CTB is also developed by adjusting the viscosity of suspending CTB before the addition of RTPF. With this approach, the splitting tensile strength increases by 68 %. The results obtained from this study pave the way for promoting the recycling of abandoned waste tyres and the safe design of backfill structures in mines.

* Corresponding author at: Department of Mechanical Engineering, Johns Hopkins University, 3400 N Charles St, Baltimore, MD 21218, USA.
E-mail address: lei.yang@sydney.edu.au (L. Yang).

https://doi.org/10.1016/j.scitotenv.2023.168320
Received 24 August 2023; Received in revised form 21 October 2023; Accepted 2 November 2023
Available online 8 November 2023

1. Introduction

Waste tyres have become a pressing environmental issue with far-reaching consequences, demanding urgent attention and innovative solutions (Mohajerani et al., 2020). It is estimated that the global annual output of end-of-life tyres reaches a staggering level (about 1.5 billion) and may reach 5 billion by 2030 due to the rapid increase in vehicle usage (Azevedo et al., 2012; Thomas and Gupta, 2016). However, the prevailing methods of waste tyres disposal, such as landfilling, stockpiling and incineration, come with significant drawbacks such as the release of toxic pollutants, air and land pollution, as well as the formation of disease sources (Dobrotă et al., 2020). Given these hazards, it is crucial to explore innovative approaches to recycle waste tyres and mitigate their impact on the environment.

The recovery of constituent materials from waste tyres, such as steel, rubber, and polymer fibre, presents a promising avenue for recycling waste tyres (Islam et al., 2022; Mucsi et al., 2018; Siddika et al., 2019). Recycled tyre polymer fibre (RTPF), as a major waste tyre recycling material, has an annual production exceeding 200,000 tons in the EU region alone and is extremely flammable and difficult to be stored safely (Baričević et al., 2018). In recent years, an increasing amount of research explored the incorporation of RTPF into the mix design of construction materials, with the objective of utilizing RTPF while preserving or even improving the engineering properties of the materials. For instance, the research team led by Zhang systematically studied the flexural (Chen et al., 2020b; Zhong and Zhang, 2020), compressive (Chen et al., 2021a; Zhong and Zhang, 2022a) and tension properties (Chen et al., 2020a; Zhong and Zhang, 2022b, 2021) of concrete or engineered geopolymer composites reinforced with RTPF. Onuaguluchi and Banthia (Onuaguluchi and Banthia, 2017), as well as Serdar et al. (Serdar et al., 2015), explored the potential of RTPF in enhancing the resistance to autogenous and plastic shrinkage of concrete. The application of RTPF in wet-sprayed concrete mixes has also been explored (Baricevic et al., 2018). Using RTPF as a filler substance in building materials has provided a sustainable solution for the recycling and utilization of RTPF (Onuaguluchi and Banthia, 2019). However, it is worth noting that there is still an urgent need to further improve the utilization efficiency of RTPF due to the increasing amount of waste tyres and the current low utilization efficiency of RTPF (Ahrens et al., 2023). This implies the exploration of application domains with a broader demand for RTPF.

Recently, applying fibres in the field of mining engineering to prepare the mine paste backfill has emerged (Yu et al., 2022). Mining activities generate extensive underground spaces known as stope or goaf while extracting valuable minerals (Chen et al., 2021a,b,c,d; Ghirian and Fall, 2013; Qi et al., 2018b). The goafs can result in pillar failure and roof collapse, which will bring significant safety hazards to underground production (Chen et al., 2023). They also may trigger surface subsidence and water inrush, causing severe casualties and huge economic losses (Chen et al., 2021a,b,c,d). In response to the growing demand of green mining practices, the implementation of cemented tailings backfill (CTB) technology is one of the prevailing solutions (Chen et al., 2017; Fall et al., 2010, 2008; Qi and Fourie, 2019). CTB is a high solid concentration (70–85 wt%) engineering composite material prepared by tailings, binder and water (Chen et al., 2018; Yin et al., 2021a). Due to its advantages in green sustainability, CTB technology has now become the mainstream in mining (Fall et al., 2010). After being prepared at the surface backfill station, the CTB is then conveyed to the stope either through gravity or pumping, serving the purpose of both surface support and waste tailings utilization (Chen et al., 2022a). Dynamic yield stress and static yield stress are two important rheological parameters and have been widely utilized for the quantitative assessment of the transportability and workability of fresh CTB. In addition, hardened CTB needs to achieve a certain level of mechanical strength to fulfill its purpose of supporting the ground surface (Chen et al., 2021a,b,c,d; Hong et al., 2023). Hence, the rheological properties (such as dynamic and static yield stress) and mechanical strength are the two pivotal characteristics of CTB (Qi et al., 2018a; Qi and Fourie, 2019; Roshani and Fall, 2020). However, hardened CTB, similar to concrete, exhibits high brittleness, poor tensile and flexural properties, and the potential for catastrophic failure (Cui and McAdie, 2023; Xue et al., 2019a). Currently, an effective solution is to incorporate polypropylene fibres (PPF) into CTB, also known as fibre-reinforced CTB (Cao et al., 2021; Libos et al., 2021; Yi et al., 2015). It is worth noting that the production of synthetic PPF entails the consumption of significant amounts of non-renewable and costly natural resources (Merli et al., 2020). The non-biodegradable nature of PPF also contributes to increased waste generation (Chen et al., 2020a). Consequently, utilizing PPF in CTB has the potential to compromise the sustainability of backfill materials, which contradicts the principles of green mining. If RTPF is proven to be effectively capable of substituting PPF in CTB, it will mark the beginning of a new era in the utilization of RTPF. The primary and immediate advantage of this breakthrough would be a reduction in the manufacture of PPF. Another enticing prospect would be the substantial increase in the utilization of RTPF. This is particularly significant considering the extensive total volume of stopes that need to be filled. The underground mines in China had a total of 1.28 billion m^3 of goaf at the end of 2015 (Yin et al., 2020). Therefore, it is imperative to assess the feasibility of employing RTPF as a viable alternative to PPF in CTB, taking into consideration the engineering properties (such as fluidity and strength) of CTB.

This study aims to comprehensively examine the influence of RTPF volume content (0.3, 0.6, 0.9, and 1.2 wt%) on the properties of CTB, including rheology, ultrasonic pulse velocity (UPV) and strength properties, to assess the feasibility of RTPF application in CTB. The mechanism of RTPF's effect on the rheological property of fresh CTB was investigated. For comparison, CTB mixtures containing PPF (0.3 wt%) were used as the reference. The microstructures of RTPF reinforced CTB and PPF reinforced CTB were characterized through scanning electron microscopy (SEM), energy-dispersive spectrometry (EDS) and mercury intrusion porosimetry (MIP). The economic and environmental impacts of incorporating RTPF into CTB were evaluated. A rheology control approach was also developed to optimize the strength performance of RTPF reinforced CTB by adjusting the rheological properties of suspending CTB before the addition of RTPF.

2. Materials and methods

2.1. Experimental materials

The raw materials used here include cement, tailings, fibres, thickener, and mixing water. Commercial PO 42.5R ordinary Portland cement (OPC) was employed as the hydraulic binder, and its particle size distribution is given in Fig. 1(a). The specific surface area (BET) and fines content (<20 μm) of OPC are 5808 cm^2/g and 66.3 %, respectively. The primary chemical composition of the binder was determined by X-ray fluorescence (XRF) analysis to be 62.34 % CaO, 21.43 % SiO_2, 5.06 % Fe_2O_3, 4.25 % Al_2O_3, 2.61 % MgO, along with other trace components. The instrument used was the PANalytical Axios 2.4 kW sequential wavelength-dispersive X-ray spectrometer with Rh anode.

The tailings utilized in this study were obtained from the Xinfang Gold Mine in Zhuanghe City, Liaoning Province, China. The particle size distribution of the tailings is illustrated in Fig. 1(a). It can be seen that the fines content of tailings is 20.55 %, which can be regarded as coarse tailings (Fall et al., 2007). The uniformity coefficient (D_{60}/D_{10}) and coefficient of curvature ($(D_{30})^2/(D_{60} \times D_{10})$) of tailings are 6.29 and 1.39, respectively. The specific gravity of tailings is 2.15. The crystalline components and morphology of the tailings are shown in Fig. 1(b) and (c), respectively. The instruments used were X-ray diffraction (XRD, Bruker D8 A25) and SEM (Zeiss Gemini 300, Germany) respectively.

The fibres used include PPF and RTPF. The as-received RTPF (Fig. 2

(a)), which was recycled from truck tyres, was provided by a waste tyre recycling company in Shandong Province, China. Due to the attachment of some rubber granules to RTPF, separation is needed to quantify the mass composition of RTPF. This study employed the sieving method described in Baričević et al. (2018), where sieves with different openings were placed on a vibrating table, allowing the separation of rubber granules and fibres through the gravitational forces. The mass proportions of cleaned RTPF and rubber granules are 57.3 % and 42.7 %, respectively. The cleaned RTPF consists of 54 % polyethylene terephthalate, 36 % polyamide 66, and 10 % polybutylene terephthalate. Fig. 2(b) shows the SEM image of RTPF. To further characterize the length distribution of RTPF (the number proportion distribution corresponding to fibres of different lengths), the image information of 600 samples was captured by a Zeiss Primotech optical microscope, and then processed by Image-Pro Plus software (version 6.0). The length distribution of RTPF is shown in Fig. 2(c). The diameter of RTPF is 20.8 (±2.3) μm obtained by a fibre diameter tester (XGD-1A, Shanghai New Fibre Instrument Co., Ltd.). The length, specific gravity and tensile strength of the selected commercial PPF are 12 mm, 0.91 and 398 MPa, respectively.

A xanthan gum with molecular weight of approximately 2.8×10^5 g/mol was used as thickener. Finally, tap water was employed as the mixing water to achieve a homogeneous mixture of OPC, tailings, and fibres.

2.2. Preparation of CTB

CTB samples with different RTPF contents (0, 0.3, 0.6, 0.9, and 1.2 wt%) were prepared, denoted as CTB0, RTP0.3, RTP0.6, RTP0.9 and RTP1.2, respectively. These RTPF contents were selected based on Xue et al. (2019a) and pre-experiments on fluidity, that is, the fresh CTB needs to have a certain fluidity after the inclusion of RTPF. PPF reinforced CTB with a fixed PPF content of 0.3 wt%, denoted as PP0.3, was prepared for comparison. Fibre content refers to the percentage of fibre volume to the total volume of dry solids (tailings + OPC). The solid content and cement-to-tailings ratio of CTB samples were fixed at 73 % and 1:6, respectively. The selected cement-to-tailings ratio is commonly used in practice for mine backfill (Xue et al., 2019b). In addition, the thickener dosages of 0.01 %, 0.05 %, 0.1 %, 0.15 %, and 0.2 %, by mass of cement, were incorporated to adjust the viscosity of the CTB mixtures. It is to be noted that the thickener was only used for RTPF reinforced CTB performance optimization and its dosage was selected based on pre-experiments of fluidity, that is, the fresh CTB needs to have a certain fluidity after the inclusion of thickener. In addition, deionized water was used to avoid the influence of free ions in solution (Zhang et al., 2022).

After the preset materials were prepared, a combination of dry and wet mixing method was adopted to maximize the uniform distribution of fibres. First, tailings, cement, and fibres were dry mixed for 3 min, then the required water (or a solution of water mixed with thickener when performing performance optimization) was added and mixed for another 5 min. The prepared samples were either directly transferred to the container for relevant fresh performance tests or placed in moulds and cured in a humidity chamber with specific temperatures (20 ± 1 °C) and relative humidity (%95 ± 1) before being tested for hardened or microstructure performances.

2.3. Tests on fresh samples

2.3.1. Flow sweep test

In this study, the dynamic yield stress of fresh CTB was evaluated using the Brookfield RSR-CC rheometer through a flow sweep test. The rheometer employed a four-bladed vane rotor, measuring 20 mm in diameter and 40 mm in length. After the pre-shearing (100 s^{-1}, 60 s), a 15-s resting was given, followed by the ramp up and ramp down steps. The duration of each ramp is 60 s and the maximum shear rate is set to 100 s^{-1}. Due to the nonlinearity of the rheological properties of fresh CTB, the data obtained from the ramp down process was analyzed by the Herschel-Bulkley (H-B) model (Eq. (1a)). Based on the obtained parameters, the equivalent plastic viscosity (μ_e) can be further obtained using Eq. (1b) (Ruan et al., 2023).

$$\tau = \tau_0 + \mu\dot{\gamma}^n \tag{1a}$$

$$\mu_e = \frac{3\mu}{n+2}\left(\dot{\gamma}_{max}\right)^{n-1} \tag{1b}$$

where τ is the shear stress. τ_0 is the dynamic yield stress. μ represents the consistency index. $\dot{\gamma}$ represents the shear rate. n represents the index indicating the degree of shear-thinning or thickening. $\dot{\gamma}_{max}$ represents the maximum shear rate employed.

2.3.2. Wet packing and water film thickness (WFT) tests

WFT was determined to study the influence mechanism of RTPF on the dynamic yield stress of fresh CTB. Based on the WFT theory (Fung and Kwan, 2010), the water introduced into the solid system can be categorized into two parts: void filling water and excess water that forms a coating film on the solid surfaces. The rationality of WFT theory in backfill materials has been confirmed and WFT is considered to be an important factor that influences the fresh property of backfill materials (Qiu et al., 2020). The WFT can be expressed by Eqs. (2a) and (2b).

$$WFT = \frac{u_0 - u_1}{A_s} \tag{2a}$$

$$u_1 = \frac{1-\rho}{\rho} \tag{2b}$$

where u_0 and u_1 are the total water volume ratio and void volume ratio, respectively, and the $u_0 - u_1$ represents the excess water volume ratio. A_s and ρ is the specific surface area and packing density of the solids, respectively. Based on the particle size distribution, the particles are

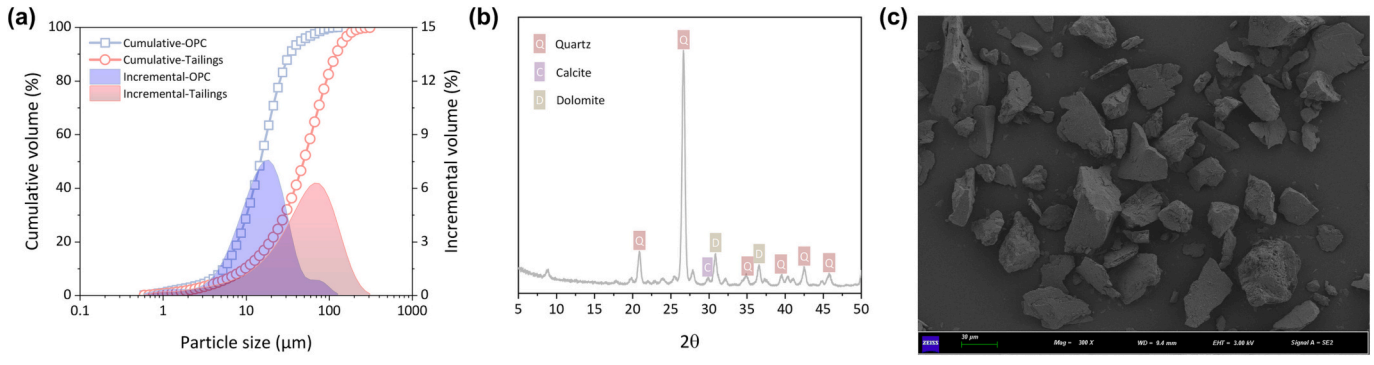

Fig. 1. (a) Particle size distribution of OPC and tailings. (b) XRD result of tailings. (c) SEM image of tailings.

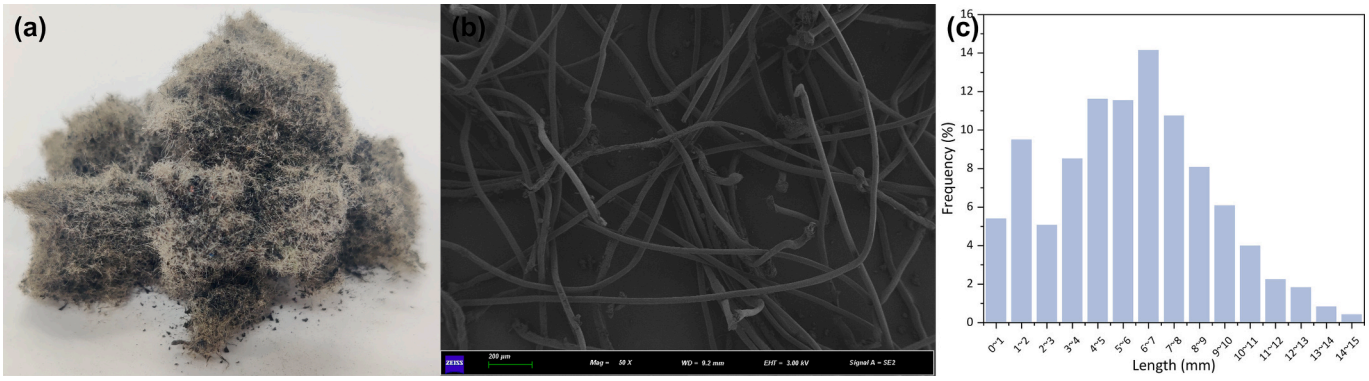

Fig. 2. (a) As-received RTPF. (b) SEM image of RTPF. (c) Length distribution of RTPF.

assumed to be spherical and then A_s can be calculated by the method described by Teng et al. (2020b).

Therefore, the acquisition of packing density is crucial in calculating the WFT. The wet packing method (Kwan and Fung, 2009) was utilized here to determine the packing density to minimize the impact of fine particle agglomeration. The packing density of the system, representing the maximum solid concentration, was determined by adding different amounts of water to the solid system and carrying out specific mixing procedures. The detailed steps of the wet packing method can be found in Qiu et al. (2020).

2.3.3. Stress growth test

The stress growth test was conducted to examine the influence of fibres on the solid-like behaviour response of CTB (Guo et al., 2023). The instrument used in this experiment is the Anton Paar MCR 302 rheometer with a concentric cylindrical geometry. To avoid the influence of strong shear on fibre orientation, no pre-shearing is performed before the stress growth test (Perrot et al., 2013). After resting for 30 s, a constant shear rate (0.01 s^{-1}) was adopted to continuously shear the sample for 60 s, which ensures the peak stress of all samples can be obtained. The obtained peak stress is regarded as the static yield stress.

2.3.4. Structural build-up test

In this study, the rheometer (Anton Paar MCR 302) mentioned above was also used. The evolutions of static yield stress and storage modulus (G') were utilized to assess the structural build-up of CTB. After reaching a certain curing age (180 s, 360 s, 900 s, 1800 s and 3600 s), the stress growth tests were carried out respectively. It should be noted that since the stress growth test is destructive, new samples need to be prepared after each test. To quantify the static yield stress evolution, the following Eq. (3) (Ma et al., 2018) was adopted:

$$\tau = \tau_{00} + \tau_f\left[1 + (\lambda_{res} - 1)e^{-t/T}\right] + A_{thix}t \quad (3)$$

where τ_{00} is the initial static yield stress. τ_f corresponds to the static yield stress of fully developed flocculation network in CTB. λ_{res} represents the degree of flocculation at the beginning of the test. T and t are relaxation time and resting time, respectively. A_{thix} is the linear evolution rate of the static yield stress.

The G' of CTB was obtained by the small amplitude oscillatory shear (SAOS) technique. Compared with the stress growth test, SAOS is a non-destructive technique. During the experiment, the CTB underwent to a sinusoidal shear strain or stress with a certain frequency, resulting in a sinusoidal stress or strain. However, due to the viscoelasticity of the material, there is a phase angle (δ) between the load and response. Fig. 3 shows a schematic diagram of the SAOS technique. The strain sweep was first performed to identify the linear viscoelastic domain (LVED). In this region, G' does not depend on the applied shear strain amplitude (Qu et al., 2023). Then the time sweep test was performed within LVED with an angular frequency of 1 Hz, which was determined by frequency sweep, to measure the G' evolution.

2.3.5. Mini V-funnel test

The flow rate of CTB mixtures was measured using mini V-funnel tests, and its value reflects the viscosity of the slurry to some extent. The version of the funnel employed here is the same as that used by Kwan and Fung (Kwan and Fung, 2012). The height of the mini V-funnel is 300 mm and the upper and lower openings are rectangles with dimensions of 30 mm × 270 mm and 30 mm × 30 mm respectively. The time it takes for the paste to flow from the beginning to completely drain out of the funnel is recorded as the flow time. Finally, the flow rate of the CTB was calculated by dividing its volume (1134 ml) by the flow time.

2.4. Tests on hardened samples

2.4.1. UPV test

A portable non-destructive digital indicating tester (Proceq Pundit Lab+) with a resolution of 0.1 μs was used to perform UPV tests. To non-destructively detect the structural state inside the sample, the UPV test was carried out on cylindrical CTB samples (Φ50 mm × 100 mm) after a predetermined curing period (28 d). It should be noted that before the UPV test, both ends of the specimen need to be polished and then coated with a thin layer of liquid Vaseline to ensure sufficient contact between transducers and the sample. The ratio between the distance between the receiver and the transmitter and the travel time of the ultrasonic pulse can be regarded as the UPV value of the specimen.

2.4.2. Mechanical tests

The cylindrical specimen after curing for 28 d was used to test for uniaxial compressive strength (UCS). The samples were tested using Humboldt HM-5030 at a deformation rate of 0.5 mm/min. The obtained stress peak value is UCS (Song et al., 2017). In addition, a linear variable differential transformer (LVDT) was placed axially in the equipment to record strain deformation in real time. The schematic diagram of the UCS test can be seen in Fig. 4(a).

The triaxial compression characteristics were evaluated using the TSZ30-2.0 based on ASTM D4767-11. The equipment utilizes has a maximum load capacity of 30 kN and is capable of applying confining pressures within the range of 0 to 2 MPa. The confining pressure (σ_2 or σ_3) set in this study were 0.2, 0.4, 0.6 and 0.8 MPa (Xue and Yilmaz, 2022), respectively. During the test, the confining pressure was initially increased to the predetermined value, followed by the application of axial strain loading (approximately 1 × 10^{-4} s^{-1}) until the specimen failed. Fig. 4(b) is a schematic diagram of the triaxial compression test.

At the predetermined curing period (28 d), the CTB specimens, with the size of Φ100 mm × 50 mm, were subjected to splitting tensile tests to determine the splitting tensile strength (STS) according to the ASTM C496. The machine used here was the same as that used for the UCS test.

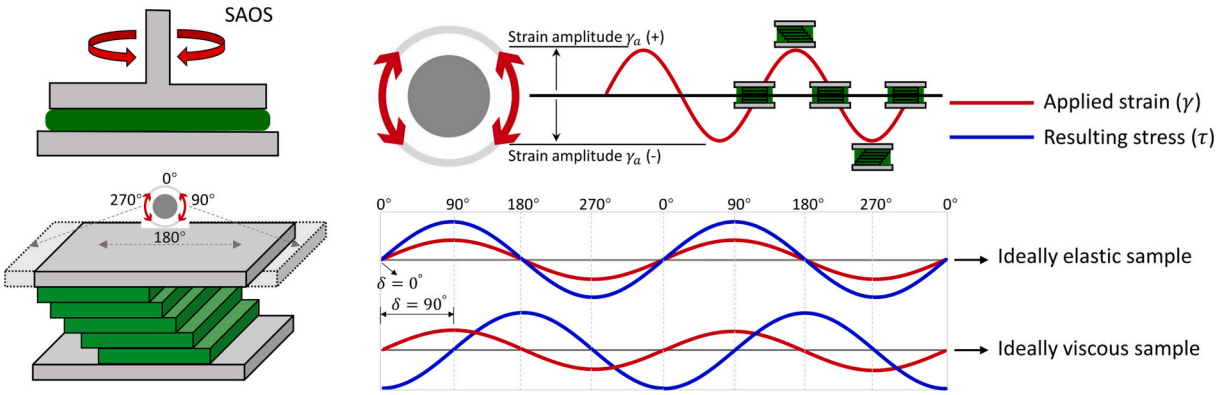

Fig. 3. Schematic diagram of SAOS technique. The parallel plate shown in the figure are for illustration purposes only. In this study, concentric cylindrical geometry was used.

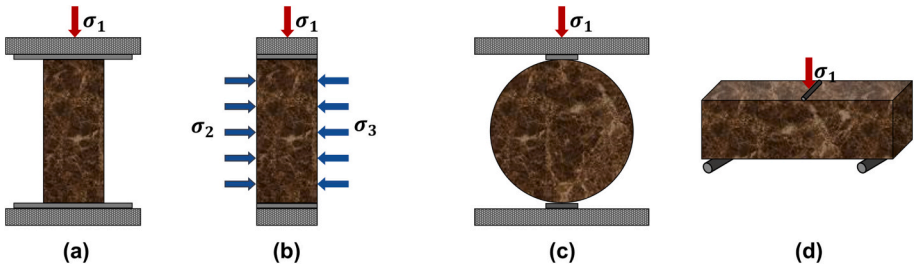

Fig. 4. Schematic diagrams of (a) uniaxial compression test; (b) triaxial compression test ($\sigma_1 > \sigma_2 = \sigma_3$); (c) splitting tensile test; (d) three-point bending test.

The tested CTB sample was positioned at the center of the bearing plate and the ball seat was appropriately adjusted to ensure that the specimen was in a reasonable load-bearing position. Subsequently, it was continuously loaded at a rate of 0.25 mm/min until the specimen was fractured. The schematic diagram of the test is shown in Fig. 4(c). In addition, the following Eq. (4) can be used to calculate STS:

$$\sigma_{STS} = q\frac{2F_{max}}{\pi DH} \quad (4)$$

where σ_{STS} represents STS. F_{max} is the maximum load during the test. D and H are the diameter and height of the specimen, respectively. q is a coefficient, here we take 1.

The flexural strength (FS) of the CTB sample was determined through three-point bending tests using the EM 1.305–2 test apparatus. This test method follows the GB/T 17671–2021. The dimensions of the beam-shaped specimen to be tested were 40 mm × 40 mm × 160 mm. As shown in Fig. 4(d), the specimen rests on two roller supports and a concentrated load is applied at its center. The experiment utilized displacement control, with a loading rate of 0.1 mm/min (Xue et al., 2019a).

2.4.3. Microstructural tests

Zeiss Gemini 300 SEM was used to observe the surface condition and bridging of fibres within the RTPF reinforced CTB and PPF reinforced CTB. The small-size samples for testing were taken from the crushed specimen after the strength tests. These samples were soaked in iso-propanol for 1 h to prevent further hydration and dried to constant weight in a vacuum oven. The gold spraying treatment was required before the SEM test. In addition, EDS was used to analyze the elemental changes of the hydration products.

A high-performance automatic mercury porosimeter (Auto-Pore V 9600) was used to analyze the pore information including pore size distribution and porosity of CTB samples. The minimum detectable pore size of this instrument is 3.5 nm, corresponding to a maximum applied pressure of 372 MPa. Similar to SEM testing, termination of hydration and drying steps are necessary before conducting the MIP test.

3. Results and discussion

3.1. Rheological properties

3.1.1. Dynamic yield stress

Fig. 5 displays the typical flow curves for all fresh CTB samples. Table 1 presents the corresponding fitting results for the H-B model. It is evident that the shear stress of all CTB samples increases continuously with the shear rate, but the rate of increase gradually diminishes (Fig. 5 (a)), reflected by a decrease in apparent viscosity (Table 1) with shear rate (Fig. 5(b)). This indicates that all fibre-reinforced CTBs exhibited a marked shear-thinning response. The fitting results of the n in H-B model, which are all <1, also confirm this (Table 1). From Table 1, it can be observed that the n of fresh RTPF reinforced CTB increases continuously with the RTPF content. This implies that the shear thinning effect of CTB is weakened by RTPF. The nature of shear thinning or shear thickening exhibited by the cement-based material under shear is dictated by the relative dominance of the shear-induced breakage over the re-aggregation of the agglomeration (Xu et al., 2020b). RTPF may enhance the agglomeration strength to a certain extent, rendering agglomerations more resistant to shear and thereby attenuating the breakage kinetics of the paste. Furthermore, it can be observed from Fig. 5(b) that RTPF reinforced CTB exhibits higher apparent viscosity compared to plain CTB under shear. Therefore, although RTPF has a significant thickening effect on fresh CTB, it does not induce a transition from shear-thinning to shear-thickening behaviour, as demonstrated in (Ruan et al., 2023), but exhibits shear thinning weakening (Luo et al., 2022).

All samples exhibit high correlation coefficients ($R^2 > 0.99$) in the H-B model fitting (Table 1). This indicates that the H-B model effectively describes the rheological behaviour of RTPF reinforced CTB and confirms its classification as a non-Newtonian fluid with yield stress. The obtained dynamic yield stress increases from 14.01 Pa (CTB0) to 33.37

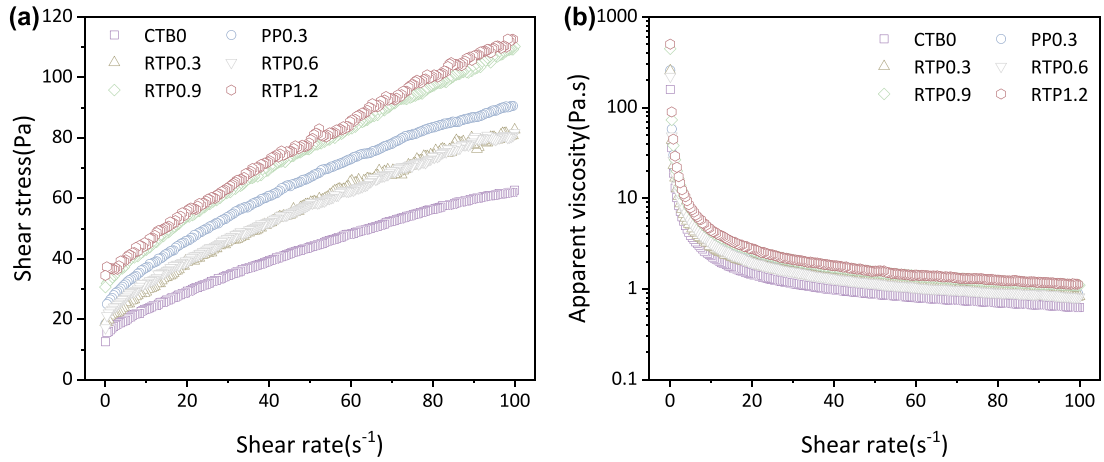

Fig. 5. Typical flow curves of all CTB samples: (a) shear rate vs. shear stress; (b) shear rate vs. apparent viscosity.

Table 1
The H-B model fitting results for all CTBs.

Sample	Model	τ_0 (Pa)	μ	n	Equivalent plastic viscosity (Pa·s)	R^2
CTB0	H-B	14.01	1.731	0.728	0.543	0.999
PP0.3		20.39	4.027	0.625	0.820	0.999
RTP0.3		16.14	2.885	0.683	0.750	0.998
RTP0.6		19.80	2.304	0.718	0.693	0.999
RTP0.9		30.18	2.385	0.761	0.862	0.999
RTP1.2		33.37	1.949	0.806	0.854	0.999

Pa (RTP1.2), indicating that the incorporation of RTPF is not conducive to the flowability of CTB. However, it should be noted that for backfill engineering practice, this degree of increase in yield stress is acceptable, as it meets the requirement that the yield stress of CTB must be <250 Pa (Jiang et al., 2019). This is also consistent with the work by Yan et al. (Yan et al., 2022), who reported that the slump of fresh CTB decreased with fibre content. The dynamic yield stress of RTP0.3 decreases by 20.84 % compared to PP0.3 (Table 1). Therefore, at the same fibre content, RTPF has a weaker deteriorating effect on the flowability of CTB than that of PPF. This can be attributed to the shorter length of RTPF and the filling effect of rubber particles (Koohestani et al., 2016; Roshani and Fall, 2020). A similar observation was also reported by Chen et al. (Chen et al., 2020b) in fresh RTPF reinforced concrete. The mechanism of RTPF on dynamic yield stress will be further discussed in Section 3.1.2. The equivalent plastic viscosities of RTPF reinforced CTBs show no significant pattern with respect to the RTPF content, which are 0.750, 0.693, 0.862, and 0.854 Pa·s, respectively. All values are higher than that of CTB0 (0.543 Pa·s). Plastic viscosity measures a material's resistance to deformation beyond its yield stress. The increase in viscosity can hinder the segregation of coarse tailings, thereby weakening the bleeding of the fresh CTB and further improving its strength evolution (Lowke, 2018). This facilitates the improvement of the roof-uncontacted problem which refers to the inadequate contact between the hardened CTB and stope roof (Zhang et al., 2020). This is one of the advantages of RTPF reinforced CTB compared to traditional CTB. In addition, the equivalent plastic viscosity of PP0.3 (0.820 Pa·s) is larger than that of RTP0.3 (0.750 Pa·s) and RTP0.6 (0.693 Pa·s). The reason for this phenomenon may be that PPF has a longer length compared to RTPF, thus forming a more complex fibre network, resulting in the equivalent plastic viscosity of PP0.3 being greater than that of RTP0.3 and RTP0.6. However, when the RTPF content exceeds 0.9 wt%, the dosage effect compensates for the length effect, making the RTPF network more pronounced. This is why RTP0.9 and RTP1.2 have larger equivalent plastic viscosity than PP0.3 (Table 1).

3.1.2. Mechanism of RTPF on dynamic yield stress

To investigate the underlying mechanism by which RTPF content affects the dynamic yield stress of fresh CTB, the concept of WFT was introduced. The WFT provides a comprehensive assessment of the water content, packing density, and solid surface area, thus being recognized as the primary determinant of the fresh properties of cement-based materials (Li and Kwan, 2013). In Fig. 6(a), the packing density and voids ratio of the mixed fibre–particle system are depicted in relation to the RTPF content. It can be seen from the figure that the packing density increases with an increase in RTPF content from 0 to 0.6 wt%, but decreases when the RTPF content increases from 0.6 to 1.2 wt%. Therefore, there exists an optimal RTPF content (0.6 wt%) that maximizes the packing density of the system. When the RTPF content is low, RTPF fills the voids between solid particles, accompanied by a decrease in voids ratio, and thus an increase in packing density (Figs. 6(a) and 7). But when the RTPF content is relatively high, some isolated RTPFs will be trapped in the narrow gaps between solid particles, which causes the particles to be wedged apart, increasing the inter-particle distance and reducing the packing density (Fig. 7) (Li et al., 2019). At this time, the voids ratio increases correspondingly with the RTPF content. This phenomenon is commonly referred to as the wedging effect (Kwan et al., 2013). The packing density determines the excess water volume available for the formation of water films that coat the solid particles, while the thickness of the water film depends on the specific surface area (Chen et al., 2019). The combined influence of total water volume, packing density, and solid specific surface area is manifested in the WFT of the RTPF reinforced CTB, as depicted in Fig. 6(b). The WFT results show that for the tested RTPF reinforced CTB samples, the WFTs are all >0 and range between 0.590 and 0.952 μm. In addition, a higher solid content corresponds to a lower total water volume, resulting in a smaller WFT. When the solid content is held constant, the WFT exhibits a trend similar to the packing density with respect to RTPF content, initially increasing and then decreasing. At an RTPF content of 0.6 wt%, the WFT reaches its maximum value for the mixture.

Fig. 6(c) illustrates the relationship between the WFT and the dynamic yield stress of RTPF reinforced CTB. It can be seen that the dynamic yield stress generally decreases as WFT. Therefore, WFT can be regarded as an important factor affecting the rheological properties of RTPF reinforced CTB. However, it is important to highlight that the CTB containing higher RTPF content exhibits higher yield stress even at the same WFT. This suggests that besides WFT, RTPF content also has a non-negligible direct and negative impact on the rheology of CTB. That is to say, unlike traditional CTB (Qiu et al., 2020), WFT is not the sole factor influencing the rheological properties of RTPF reinforced CTB. As mentioned above, RTPF affects the packing density of the solid system through the filling and wedging effects and thus changes the excess

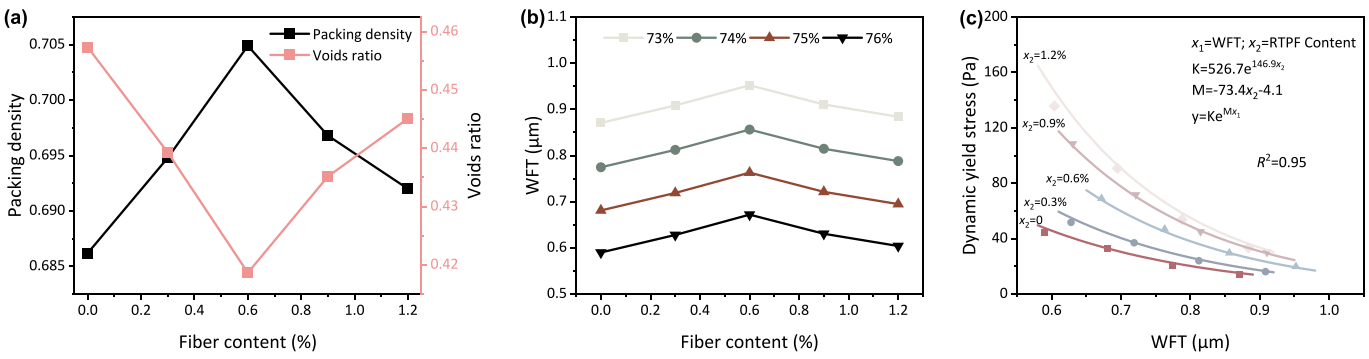

Fig. 6. (a) Effects of RTPF content on packing density and voids ratio. (b) WFT variation with RTPF content and solid content. (c) Correlation of dynamic yield stress to WFT and RTPF content.

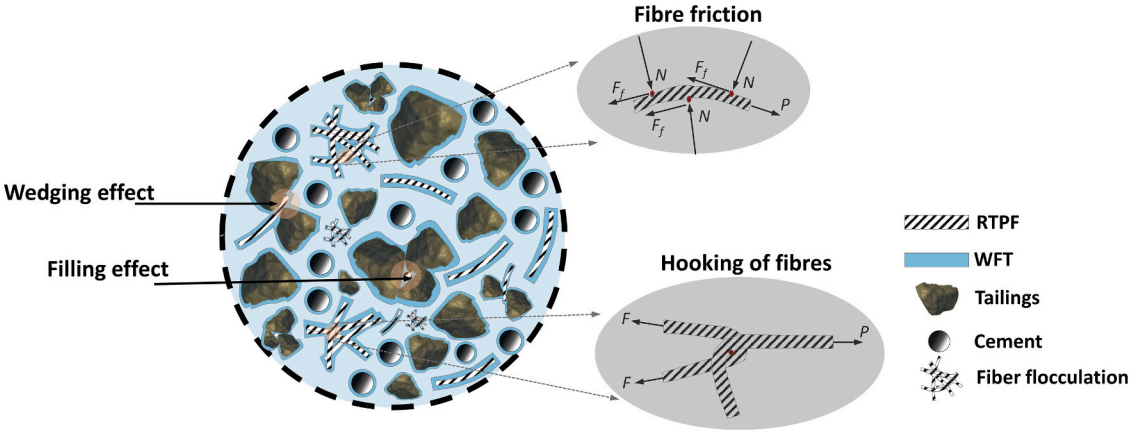

Fig. 7. Illustration of the mechanism of RTPF affecting dynamic yield stress. P is the cohesive force. F is the hooking force. F_f is the frictional force. N is the normal force.

water content, which can be reflected by the WFT and regarded as the indirect effect of RTPF. On the other hand, RTPF does deform under paste consistency, which leads to fibre interlocking and the formation of fibre flocculation (Sultangaliyeva et al., 2020) (Fig. 7). Due to the hooking force (F) generated by the mechanical entanglement of RTPFs and the frictional force (F_f) caused by the normal forces (N) at the fibre contact points, RTPF flocculation has mechanical strength and can withstand certain external loads, thereby increasing the dynamic yield stress of RTPF reinforced CTB (Fig. 7) (Bennington et al., 1990). According to the WFT theory, the effect of RTPF flocculation cannot be reflected by WFT and can be interpreted as the direct effect of RFPT on the rheological properties of CTB. This underscores the limitations of the aforementioned WFT as the sole determinant of the dynamic yield stress of RTPF reinforced CTB. In addition, as depicted in Fig. 6(c), it is evident that the dynamic yield stress of RTPF reinforced CTB increases continuously with RTPF content, without displaying a reversed V-shaped trend observed in WFT with RTPF content (Fig. 6(b)). This means that while WFT and the direct effect of RTPF jointly influence the dynamic yield stress of RTPF reinforced CTB, the latter plays a dominant role.

To consider the combined effect of WFT and RTPF content, the dynamic yield stress can be regarded as a multivariable function of WFT and RTPF content. According to (Guo et al., 2021), the dynamic yield stress of fresh CTB without RTPF added can be related to the WFT by a simple function in the form of:

$$y = Ke^{Mx_1} \tag{5}$$

where y is the dynamic yield stress, x_1 represents WFT. K and M are related constants. After RTPF is incorporated, it is assumed that the direct effect of RTPF can be reflected by K and M, that is, K and M are functions of RTPF content. Then the Eq. (5) becomes:

$$y = f(x_2)e^{g(x_2)x_1} \tag{6}$$

where x_2 represents RTPF content. f and g are single-variable functions of x_2, representing the direct effect of RTPF on the dynamic yield stress. When RTPF is not incorporated ($x_2 = 0$), Eq. (6) can be reduced to Eq. (5).

Finally, Eq. (6) was used to perform regression analysis on the rheological data, and the dynamic yield stress model of RTPF reinforced CTB was obtained as:

$$y = \left(526.7e^{149.6x_2}\right)e^{(-73.4x_2-4.1)x_1} = 526.7e^{149.6x_2-73.4x_1x_2-4.1x_1} \tag{7}$$

The results of the regression analysis indicate a strong correlation with an R^2 of 0.95 (Fig. 6(c)). This implies that the dynamic yield stress of RTPF reinforced CTB is predominantly controlled by WFT and RTPF content, and the direct effect of RTPF can indeed be captured by Eq. (7). The obtained optimal regression equation provides insight into the effects of WFT and RTPF content on the rheological properties of RTPF reinforced CTB. But on the other hand, this model is semi-empirical and has certain application limitations. Based on Eq. (7) ($y = 526.7e^q$), one straightforward way for designing RTPF reinforced CTB to achieve a desired dynamic yield stress involves first determining the maximum $q(x_1, x_2)$ needed. Next, the WFF and RTPF content should be adjusted to attain a target q value by increasing WFT or decreasing RTPF content. However, there exists an upper limit to the WFF since increasing it would adversely affect the strength due to the associated increase in the water to cement ratio. Similarly, there is a lower limit to the RTPF content below which the contribution of fibres in enhancing the hardened properties of RTPF reinforced CTB, especially the tensile and

flexural strength, would be reduced.

3.1.3. Static yield stress and structural build-up

Here we compared the effect of PPF and RTPF on the static yield stress and G′ of CTB. It should be noted that for RTPF, we only selected the RTPF content (0.6 wt%) corresponding to the maximum packing density of the system to facilitate comparison. Fig. 8(a) compares the static yield stress evolutions of RTP0.6 and PP0.3 against that of CTB0. Table 2 shows the thixotropic parameters of the static yield stress evolution fitted by Eq. (3). The discrepancy in the evolution of static yield stress among the three CTBs is evidently substantial. Compared to CTB0, both PPF and RTPF result in an elevation of the static yield stress, thanks to the enhanced agglomeration strength provided by the fibres. The static yield stress of CTB0 and RTP0.6 shows a linear evolution, while the PP0.3 sample exhibits a structural build-up kinetic that first evolves sharply with a relaxation time of 421.96 s and then increases linearly. Due to thixotropy, fresh cement-based material at rest can undergo re-flocculation and be brought back to an initial reference state after strong mixing (Xin et al., 2022). This process corresponds to the rapid evolution stage of static yield stress (Ma et al., 2018). Therefore, it indicates that the thixotropy of the fresh CTB is not strong, which can be attributed to its high water and inert tailings contents. In addition, the enhancement effect of RTPF on the thixotropy of CTB is not significant, as evidenced by the linear evolution of static yield stress of RTP0.6 throughout. The A_{thix} of RTP0.6 is higher compared to CTB0, as shown in Table 2. This is in accordance with Perrot et al. (2013), where a certain amount of fibres can enhance the structural build-up rate. However, PPF leads to a similar A_{thix} as CTB0.

To gain a comprehensive understanding of the underlying interactions that contribute to the structural build-up, we will examine the LVED, G′ and the evolution of shear stress presented in Fig. 8(b), (c) and (d), respectively. Fig. 8(b) shows the strain sweep results of different samples. It is evident that PP0.3 exhibits the highest G′, followed by RTP0.6, while CTB0 demonstrates the lowest value. This corresponds to the static yield stress results. In addition, there is no significant difference in the critical strain corresponding to the end of the LVED of these samples, with all values approximately 0.0001, which is equal to the critical strain of pure cement paste (Ma et al., 2018). The disruption of the hydration product links at pseudo-contact zones between particles, which are preferential nucleation sites, is responsible for the critical strain (Roussel et al., 2012). This suggests that the incorporation of PPF or RTPF does not modify the distance between pseudo-contact regions, thus exerting no influence on the quantity of pseudo-contract points and ultimately leading to negligible alterations in cement hydration. This is consistent with the evolution of G′ depicted in Fig. 8(c), where all 3 samples exhibit comparable G′. Therefore, it can be inferred that the mechanism by which PPF and RTPF influence the static yield stress of CTB is not through affecting cement hydration. The shear stress evolution of the sample during the strain sweep is shown in Fig. 8(d). It can be seen that the critical strain at the onset of flow for PP0.3 is

Table 2
Thixotropic parameters of CTB0, PP0.3 and RTP0.6.

Sample	τ_{00} (Pa)	τ_f (Pa)	T (s)	A_{thix} (Pa/s)
CTB0	24.02	–	–	0.098
PP0.3	62.60	139.54	421.96	0.097
RTP0.6	31.66	–	–	0.125

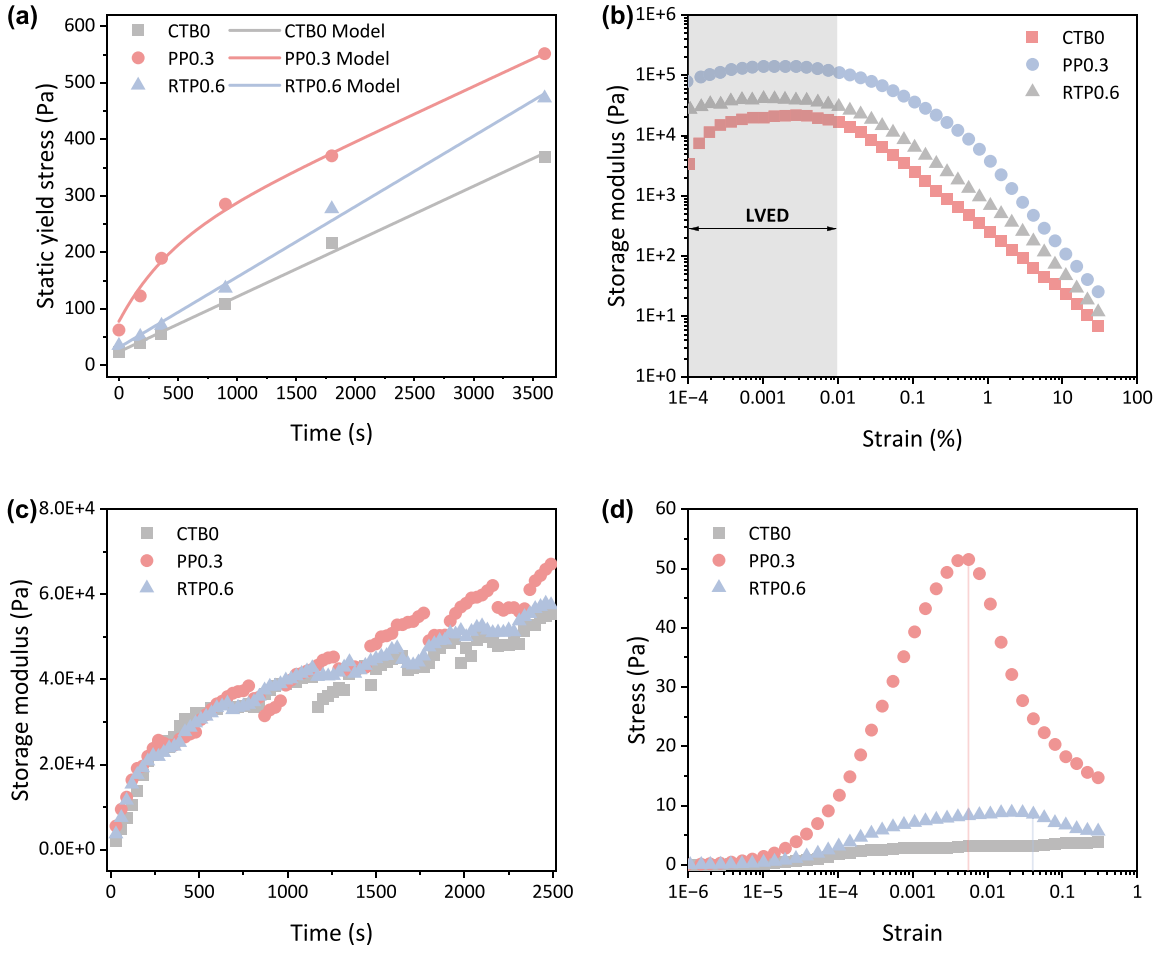

Fig. 8. (a) Static yield stress evolution; (b) LVED; (c) Storage modulus evolution; and (d) shear stress evolution of CTB0, PP0.3 and RTP0.6.

approximately the same as that of CTB0, but the corresponding shear stress is much higher. This critical strain involves non-contact interactions between particles, controlled by colloidal flocculation (Roussel et al., 2012). Hence, the inclusion of PPF can strengthen the flocculation in CTB, thereby leading to enhanced thixotropy. The CTB incorporating 0.6 wt% RTPF exhibits a peak shear stress at a strain of approximately 0.02, surpassing the corresponding value observed in CTB0. The cause of this phenomenon can be attributed to the wedging effect of RTPF, as described in Section 3.1.2. In addition, the higher RTPF content contributes to the enhancement of the magnitude of the spatial congestion within the fibre network (Lecompte and Perrot, 2017). This interaction in the fibre network caused by the interpenetration and entanglement of RTPF is the origin of the greater A_{thix} of RTP0.6. A similar effect has been observed in fresh cement pastes incorporating diutan gum (Ma et al., 2018).

3.2. Mechanical properties

3.2.1. Uniaxial and triaxial compressive strengths characteristics

Fig. 9(a) presents the UCS results of all samples. The result of UPV is also illustrated for comparison as the UCS of the backfill material is strongly related to its UPV (Ma et al., 2018). It can be observed that only PP0.3 and RTP0.6 exhibit a higher UCS compared to CTB0, with increases of 4.62 % and 6.33 % respectively. This finding implies that the reinforcing effect of fibres on the UCS of CTB is manifested only at appropriate dosage levels. When the fibre content is 0.3 wt%, the UCS of PPF reinforced CTB (1.56 MPa) exceeds that of RTPF reinforced CTB (1.47 MPa). However, as the RTPF content is further increased to 0.6 wt %, RTP0.6 achieves a higher UCS (1.59 MPa). For RTPF reinforced CTB, the UCS exhibits a trend of initially increasing and then decreasing with RTPF content, reaching its maximum at 0.6 wt% RTPF content. Moreover, increasing the RTPF content from 0.6 to 1.2 wt% results in a corresponding decrease in UCS from 1.59 MPa to 1.38 MPa. Hence, 0.6 wt% can be regarded as the critical RTPF content for enhancing the UCS of CTB. Compared to concrete, CTB exhibits a higher water content and a lower binder dosage (Douara et al., 2022; Kanta and Ponnada, 2022; Khial and Chaid, 2022; Roshani and Fall, 2020). Consequently, the hardened CTB possesses a more porous and looser characteristic due to the evaporation of water (Ghirian and Fall, 2013) and the insufficient formation of hydration products such as C-S-H (Qiu et al., 2020). However, the deformed RTPF effectively fills the voids in the CTB, resulting in increased specimen compactness and thus an improved UCS (Chen et al., 2019). This is further supported by the UPV results, as shown in Fig. 9(a), where the addition of fibres (0.3–0.6 wt%) enhances the UPV of the samples, indicating a reduction in voids ratio (Xue and Yilmaz, 2022). Furthermore, the observed pore structure characteristics align with this result, which will be discussed in detail in Section 3.3. The structural difference between CTB and concrete is the reason for the different variations in UCS with RTPF content. In the case of concrete, the UCS decreases continuously with RTPF content (Chen et al., 2020a). Once the critical RTPF content is exceeded, on one hand, the wedging effect of fibres leads to a decrease in the packing density of the system (Figs. 6(a) and 7). On the other hand, the increased trapped air content in RTPF results in an increase in porosity (Chen et al., 2020a) and the emergence of weak structure surfaces within the matrix (Xue et al., 2019a). Under the combined effect of these two factors, the UCS of the specimens decreases. The UPV results are also in agreement with UCS results within this range of RTPF content (0.6 wt%-1.2 wt%). Some studies have established empirical equations for UPV and UCS of concrete (Demirboğa et al., 2004) or CTB (Xu et al., 2020a), but attempts for

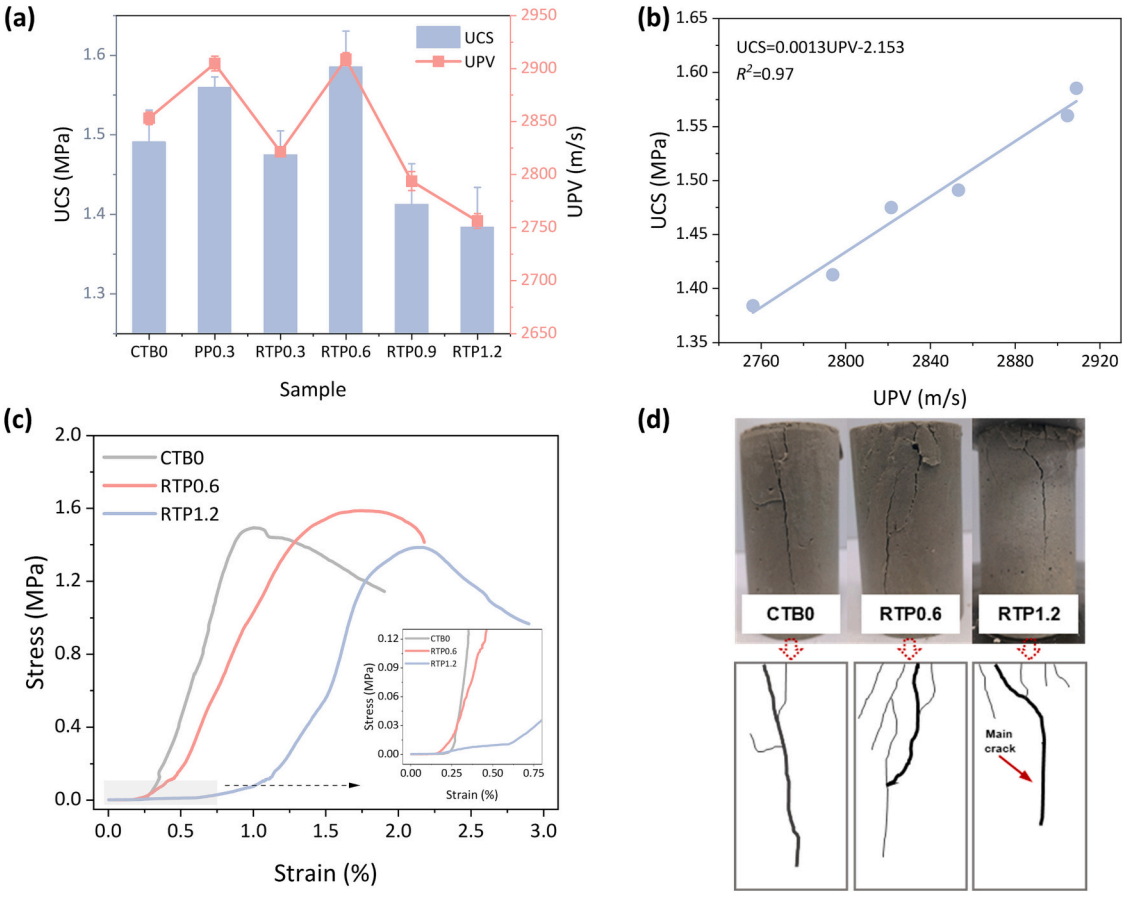

Fig. 9. (a) UCS and UPV results of samples. (b) Relationship between UCS and UPV of fibre-reinforced CTB. (c) Typical stress-strain curves for unconfined compression tests of samples. (d) Crack patterns of samples.

RTPF reinforced CTB are limited. The results of Fig. 9(b) demonstrate a strong linear correlation between UCS and UPV of fibre-reinforced CTB, with a high R^2 of 0.97. Therefore, the UCS of RTPF reinforced CTB can also be reliably predicted using UPV, but more samples need to be tested to ensure a more accurate relational model.

Fig. 9(c) shows the stress-strain curves of CTBs with and without RTPF inclusion of UCS tests. Fig. 9(d) illustrates the damage patterns of CTB0, RTP0.6, and RTP1.2 when reaching their respective ultimate strengths. It can be seen from Fig. 9(c) that RTPF contributes to improving the stress-strain curve of CTB. For CTB0, the stress drops dramatically after reaching the peak point. This reflects the brittleness of CTB0, which is also confirmed by the crack pattern in Fig. 9(d). This specimen is dominated by through-tensile failure parallel to the direction of axial compression, in which main cracks are generated, and secondary micro-cracks are relatively few. When RTPF content is the optimal dosage (0.6 wt%), RTPF exerts a tensile effect, and the specimen exhibits a macroscopic shear failure. In this case, the post-peak stress-strain curve becomes flat, indicating the transition of the sample from brittle to ductile. When the RTPF content is further increased to 1.2 wt%, the initial concave stage of the stress-strain curve (called the pore compaction stage (Yang et al., 2020)) is prolonged attributed to the decrease of packing density and the increase in air content. In addition, the post-peak stress evolution is similar to that of CTB0, indicating that a larger RTPF content does not necessarily mean a more pronounced ductile characteristic of RTPF reinforced CTB. In this case, the specimen exhibits a hybrid (tensile-shear) failure mode, with the two main cracks mutually penetrated. A similar failure pattern was also observed by Xu et al. in CTB at different curing temperatures (Xu et al., 2020a).

Based on the UCS results, it can be observed that the highest UCS of CTB can be achieved when the RTPF content is 0.6 wt%. Therefore, only CTB0, PP0.3, and RTP0.6 were selected for triaxial compression test for the purpose of comparison in this study, and the results are shown in Table 3. The 2, 4, 6, and 8 in the specimen number correspond to the confining pressures of 0.2, 0.4, 0.6, and 0.8 MPa, respectively. As expected, the peak axial strength (σ_1) of the sample is much larger than UCS. This is because the specimen cannot expand freely in the transverse direction due to lateral constraints (Yang et al., 2020). The σ_1 and residual strength (σ_{res}) of the specimens both increase with confining pressure, and the difference between them becomes smaller (i.e., the η value approaches 1). Numerically, the η value of CTB0 is much smaller than that of fibre-reinforced CTB, which is closer to 1. This demonstrates the transition of CTB0 from brittle to ductile behaviour under the influence of confining pressure and the enhancement of CTB's toughness characteristics through the incorporation of fibres. To further assess the impact of confining pressure on the triaxial stress state of the specimens, the confining pressure effect index (θ) (Xue and Yilmaz, 2022) was employed. It is evident that θ decreases gradually with confining pressure, and the θ of CTB0 is greater than that of fibre-reinforced CTB. This suggests that the strengthening effect of confining pressure on the σ_1 of non-fibre-reinforced CTB is stronger than that of fibre-reinforced CTB. A similar observation was also reported by Xue et al. (Xue and Yilmaz, 2022). In addition, both σ_1 and θ of RTP0.6 are larger than those of PP0.3. Consequently, similar to the UCS results, RTP0.6 demonstrates superior triaxial properties compared to PP0.3.

Table 3
Summary of triaxial compressive test results of samples.

Sample	σ_1 (Pa)	σ_{res} (Pa)	η[a]	θ[b]
CTB0-2	2.356	1.639	0.696	4.323
CTB0-4	3.159	2.404	0.761	4.169
CTB0-6	3.742	3.097	0.828	3.752
CTB0-8	4.351	3.829	0.880	3.575
PP0.3-2	2.370	1.852	0.782	4.050
PP0.3-4	3.032	2.621	0.864	3.679
PP0.3-6	3.563	3.221	0.904	3.339
PP0.3-8	4.126	3.989	0.967	3.208
RTP0.6-2	2.404	2.148	0.893	4.071
RTP0.6-4	3.078	2.941	0.955	3.721
RTP0.6-6	3.651	3.413	0.935	3.435
RTP0.6-8	4.274	4.145	0.970	3.355

[a] $\eta = \sigma_{res}/\sigma_1$.
[b] $\theta = (\sigma_1 - \mathrm{UCS})/\sigma_3$.

3.2.2. Splitting tensile and flexural strengths characteristics

Fig. 10(a) shows the STS results of CTBs with and without fibres. The results of CTB0 are highlighted with a red dashed line for comparison. It is observed that not all fibre-reinforced CTBs exhibit higher STS than that of CTB0. Among the tested specimens, only PP0.3 (0.319 MPa), RTP0.3 (0.325 MPa), and RTP0.6 (0.324 MPa) demonstrate greater STS than that of CTB0 (0.328 MPa). The enhancement of STS can be attributed to the bridge effect of fibres across the fracture zone (Fig. 10 (b)), which inhibited the initiation and propagation of cracks (Chen et al., 2020b). However, this improvement is not significant overall, which can be attributed to the high water-cement ratio of CTB, leading to poor bonding between the matrix and fibres. In addition, the hydrophobic characteristics of PPF and RTPF may also be one of the reasons (Chen et al., 2020a). Under the coupling effect of these two factors, the fibre may experience slippage or pull-out as the cracks propagate, ultimately leading to a decrease in the tensile capacity of the sample (Chen et al., 2020a). At the same fibre content of 0.3 wt%, the STS of RTPF reinforced CTB is slightly lower than that of PPF reinforced CTB. The reason may be the loss of fibre bridging efficiency due to the short fibre length of RTPF as shown in Fig. 2(c). As for the effect of RTPF content on the STS, incorporating 0.3–1.2 wt% RTPF can increase the STS up to 2.73 % as compared with CTB0. Similar to the results of UCS, there is also a critical RTPF content (0.6 wt%). As the RTPF content increases below this threshold, the STS also increases due to the improvement of interlocking force and bonding strength caused by the increase of fibre number density and the contact area between fibres and matrix. Subsequently, the further incorporation of RTPF will weaken the STS. This phenomenon can be attributed to the formation of a weak interface between fibres and CTB matrix due to the significant entrapped air carried by the higher content of RTPF (Cao et al., 2021). A similar observation was also reported in cemented sulfur tailings backfill containing PPF (Yin et al., 2021b).

Fig. 10(c) depicts the load-displacement curves of samples (CTB0, RTP0.3, RTP0.6 and RTP1.2). All load-displacement curves can be divided into three stages (Fig. 10(c) inset). Firstly, similar to the uniaxial compression curve, the specimen also undergoes an initial stage of pore compaction followed by a nearly linear elastic stage (OA). Due to the rise in packing density, the initial compaction stage of RTP0.3 and RTP0.6 is shortened. In addition, RTPF reinforced CTB exhibits a softening feature before the peak, with the curve transitioning from “linear” to “upward concave”. Upon reaching the peak load, the curve plummets, followed by entering the BC stage. Comparison to CTB0, RTPF reinforced CTB exhibits lower load drop and smoother transition. This observation suggests that RTPF enhances the ductility of CTB. The damaged specimens still retain a certain residual strength, and the curve starts to decline into the CD phase after reaching the second peak load. It is worth noting that all specimens exhibit a similar failure mode, but more secondary cracks can be observed near the loading end of RTPF reinforced CTB (Fig. 10(d)). The reason for this phenomenon is the increased stress concentration between the sample and the loading positions, which also reflects the enhancement of the ductility of the CTB by the RTPF (Chen et al., 2020a).

The FS of specimens is also presented in Fig. 10(a). The FS of CTB is generally improved by incorporating RTPF, regardless of the dosage of fibre present. As compared to the plain reference sample CTB0, the FS of RTP0.3, RTP0.6, RTP0.9, and RTP1.2 increase by 7.86 %, 21.60 %, 9.65 %, and 2.23 %, respectively. The enhanced resistance to crack development across the fracture zone is considered to be the cause of the improvement in FS and this enhancement effect is influenced by fibre

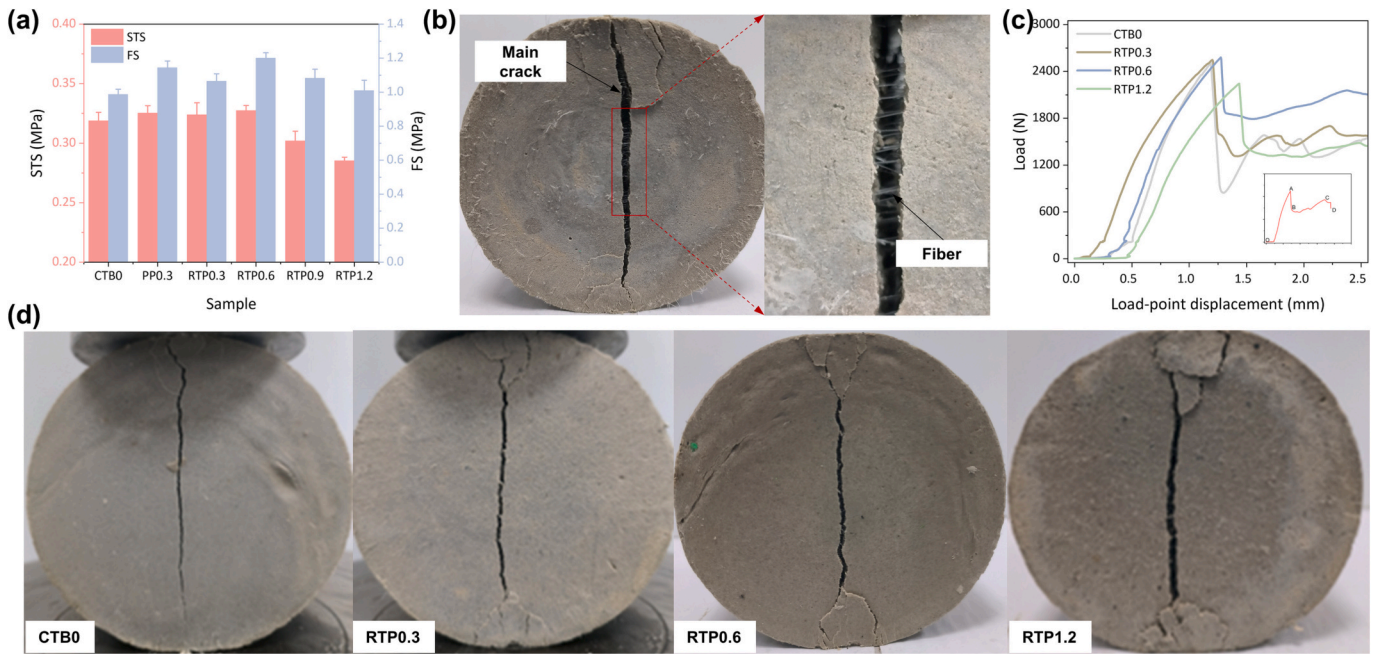

Fig. 10. (a) STS and FS results of all samples. (b) The fibre bridging effect. (c) The load-point displacement curves of splitting tensile tests and (d) crack patterns of specimens (CTB0, RTP0.3, RTP0.6 and RTP1.2).

content and orientation (Chen et al., 2020b). Additionally, it can be observed in Fig. 10(a) that the highest FS is achieved by RTP0.6. However, the continuous addition of RTPF (i.e., 0.9 wt% and 1.2 wt%) weakens the positive effects provided by the RTPF, resulting in approximately 9.82 % and 15.93 % reduction in FS, respectively, compared to that of RTP0.6. This performance can be attributed to an excessive content of RTPF, which results in poor distribution of fibre that further weakens the fibre-matrix bonding, consequently reducing the efficiency of fibre bridging (Chen et al., 2020b). Finally, the FS of PP0.3 is 7.49 % higher than that of RTP0.3 but lower than the value of RTP0.6. This can also be attributed to the difference in length between RTPF and PPF, where longer fibres exhibit superior crack-bridging capability.

3.3. Microstructural properties

Fig. 11 illustrates the pore structure characteristics of samples CTB0, PP0.3 and RTP0.6. The porosity for CTB0, PP0.3, and RTP0.6 are 43.99 %, 41.46 %, and 40.16 % respectively (Fig. 11(a)). Therefore, the incorporation of fibres can significantly reduce the porosity of CTB. This is in good agreement with the packing density (voids ratio) and can explain the strength variation of the specimen to some extent. To conduct a more detailed analysis of the pore distribution, the pores in the sample are categorized into four types: gel micro-pore (< 10 nm), transition pore (10–100 nm), capillary pore (100–1000 nm), and large pore (> 1000 nm) (Jin et al., 2017). The pore size distribution is shown in Fig. 11(b). It can be found that the main pore type of CTB or fibre-reinforced CTB is large pores, accounting for 58.10 % to 65.18 % of the total pore volume, followed by capillary pores and transition pores, with gel micro-pores being the least. The incorporation of PPF (0.3 wt%) and RTPF (0.6 wt%) significantly reduces the large pore proportion while substantially increasing the proportion of transition pore. This further demonstrates that an appropriate fibre content helps refine the pores through fibre filling, resulting in a denser CTB mixture. A similar conclusion that fibres can refine the pore structure was also obtained in alkali-activated slag mortar (Xu et al., 2021). Since capillary pores and large pores are the main factors detrimental to the strength properties of backfill materials (Chen et al., 2022b), the reduction of porosity and the large pore proportion are the reasons for the increase in strength of fibre-

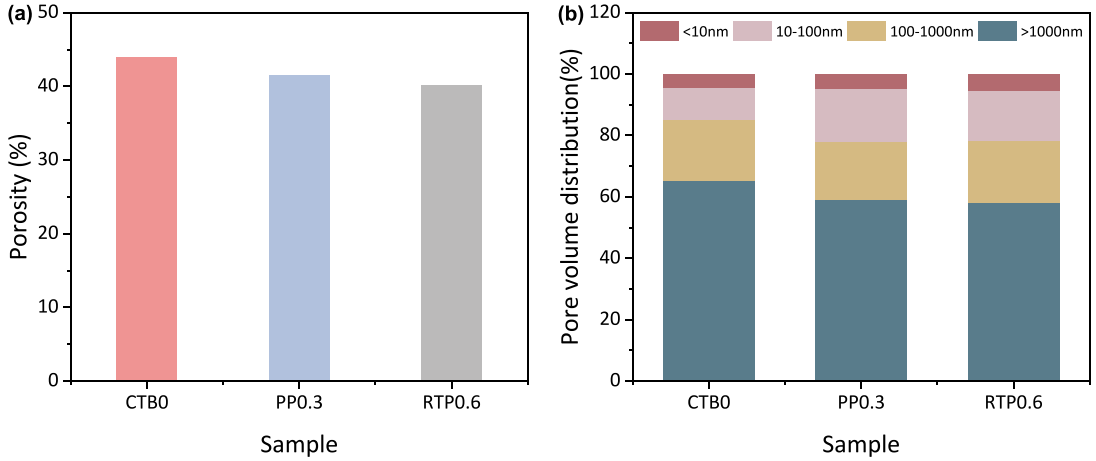

Fig. 11. Pore structure characteristics of samples: (a) porosity; (b) pore size distribution.

reinforced CTB. The major difference between PP0.3 and RTP0.6 lies in the gel pore, with RTP0.6 exhibiting a 13.71 % higher proportion of gel pore than PP0.3. Moreover, the proportion of large pore in RTP0.6 experiences a slight reduction (1.50 %) compared to PP0.3. These observations provide an explanation for the superior strength properties of RTP0.6 over PP0.3.

The surface condition of samples (CTB0, PP0.3 and RTP0.6) after strength tests were analyzed by SEM, as shown in Fig. 12. It can be clearly seen that some cracks are present in CTB0 (Fig. 12(a-1) and (a-2)), while no cracks are observed in fibre-reinforced CTB. This is consistent with the strength results and also demonstrates the inhibitory effect of fibres on internal cracks. In addition, it can be found from Fig. 12(b-1) and (c-1) that there is a gap between fibre and matrix, whether it is RTPF or PPF. This reflects the poor mechanical performance of CTB compared to concrete (Arunachalam et al., 2021; Arunkumar and Muthiah, 2022; Chen et al., 2020b; Kanta and Ponnada, 2022), where fibres can effectively penetrate into the matrix. The high water-cement ratio of CTB is responsible for this phenomenon. Therefore, compared with chemical bond, frictional bond is the main factor affecting the pull-out process of fibres in CTB. From Fig. 12(b-2) and (c-2), it can be observed that PPF exhibits significant deformation and scratches after fibre pull-out, while the surface of RTPF remains relatively intact. This means that RTPF may have a higher load-bearing capacity than PPF if only the surface condition of fibres is considered. This is consistent with the conclusions of Chen et al. (Chen et al., 2019). Fig. 12(a-3), (b-3) and (c-3) show the EDS results of the samples. Ca, Al and Si are the main elements in the formation of hydration products (such as C-S-H, CH and Aft), while Mg mainly affects the early mechanical strength (Xue et al., 2019b). It can be seen from the figure that for CTB0, PP0.3 and RTP0.6, the total weight percentages of Ca, Al, Si and Mg are 37.7 %, 43.75 % and 43.93 %, respectively. This is consistent with the strength results that CTB0 has the smallest strength while PP0.3 and RTP0.6 have comparable mechanical strength. Xue et al. (Xue et al., 2019b) obtained similar conclusions in their study on cement-tailings matrix composites using SEM-EDS analysis.

3.4. Economic, environmental and mechanical properties comparison

This section primarily discusses whether PPF can be replaced by RTPF in CTB from multiple perspectives, including life-cycle cost, embodied carbon (EC), embodied energy (EE), and mechanical properties (dynamic yield stress and strength, etc.), where EC and EE can be considered as material sustainability indicators reflecting the environmental impact of CTB (Zhong and Zhang, 2021). The unit cost, EC, and EE of the ingredients required for CTB preparation are summarized in Table 4 (M. Chen et al., 2021b; Du et al., 2022; Li et al., 2021; Norgate

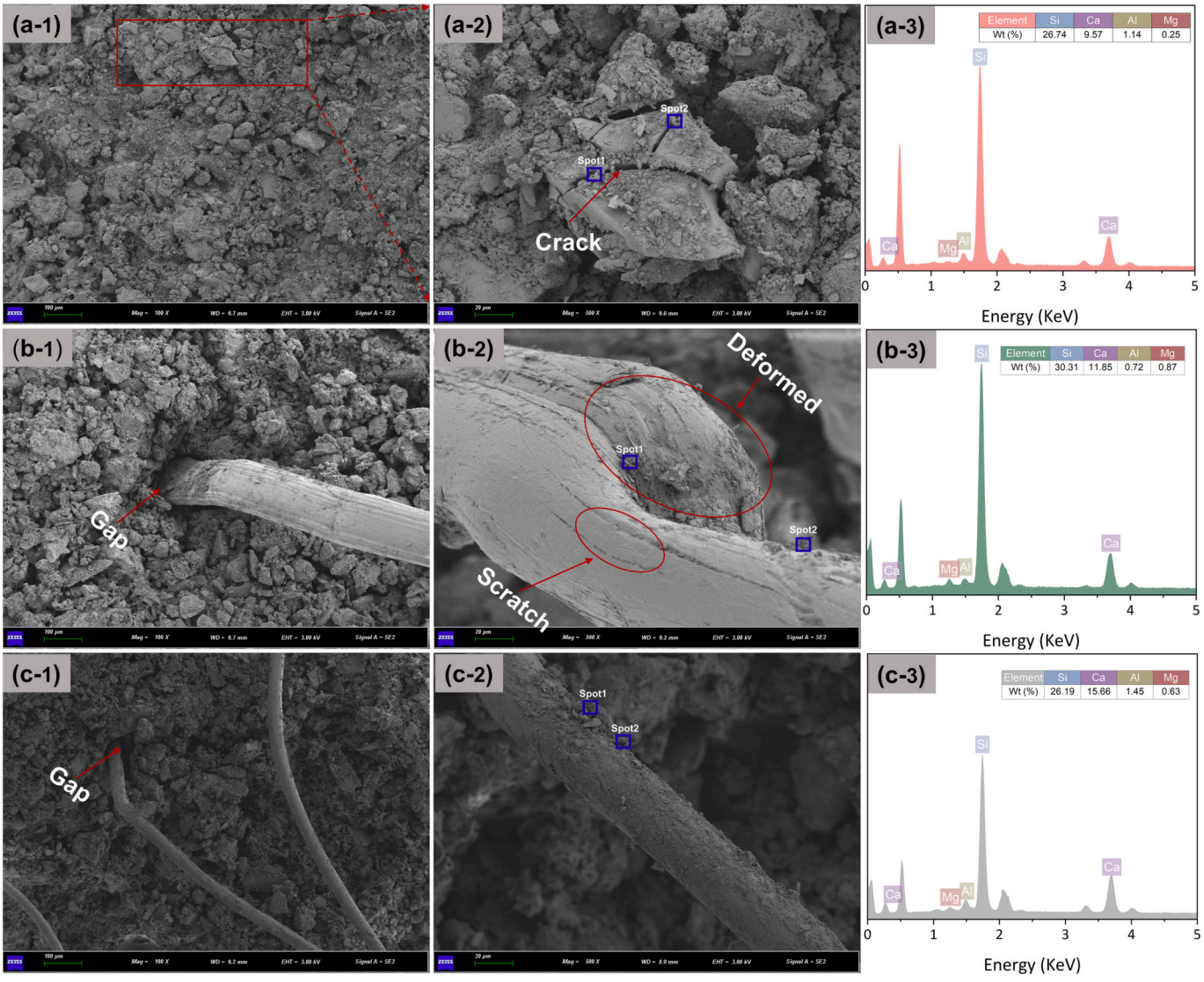

Fig. 12. SEM results of various CTB samples: (a) CTB0; (b) PP0.3; (c) RTP0.6.

and Haque, 2010; Zhong and Zhang, 2021). According to the inventory data in the table, the estimated results of all samples are presented in Fig. 13(a). All index values of CTB0 are set as 1 and results for fibre-reinforced CTB are displayed as the ratio to the corresponding original value of CTB0. The obtained unit material cost, EC and EE of CTB0 are 12.54 USD/m^3, 168.37 kg CO_2·eq/m^3 and 1129.38 MJ/m^3 respectively. The figure illustrates that the incorporation of PPF (0.3 wt%) significantly increases the total material cost of CTB, with an increase of 287.11 % compared to CTB0. The total cost after adding RTPF (0.3–1.2 wt%) increases with the RTPF content, and its increase ranges from 14.36 % to 56.92 %. Such a large cost reduction can be attributed to the exceptionally low market price of RTPF, which is only 5.10 % that of PPF. In addition, the magnitude of change in EC of fibre-reinforced CTB is significantly weaker than that of cost, and the increase is in the range of 5.22–20.67 % compared to CTB0. It is noteworthy that there is no significant difference (approximately 5.30 %) in the increase percentage of EC between PP0.3 and RTP0.3, which can be mainly ascribed to the comparable unit EC of PPF and RTPF. The EC of RTP0.6 is 185.89 kg CO_2·eq/m^3, which is only 4.65 % higher than that of PP0.3. As for EE, PP0.3 exhibits the maximum value (1492.85 MJ/m^3), approximately 32.18 % higher than that of CTB0. The EE of RTPF reinforced CTB increases gradually with RTPF content (0.3–1.2 wt%) and the increase is in the range of 6.83–27.04 % compared to CTB0. Taken together, using RTPF to replace PPF in CTB has the potential to greatly improve its sustainability, especially the cost. However, it should be noted that rubber materials may degrade and accelerate the aging process in an alkaline environment. Therefore, the durability and potential risks of RTPF reinforced CTB to the environment need to be considered during the long-term service of the material. This is what needs to be studied and solved in the future.

Fig. 13(b) plots the cost, EC, EE, dynamic yield stress and strength of all samples for a more comprehensive evaluation. In the radar chart, a smaller area represents better comprehensive performance with lower cost, better sustainability and mechanical properties (Du et al., 2022). The radar chart areas of different samples are depicted in Fig. 13(c). It is evident that RTPF reinforced CTB exhibits superior comprehensive performance compared to PP0.3. It is crucial to strike a balance between reducing costs, EE, and EC without compromising mechanical properties. From Fig. 13(b), it can be observed that RTP0.6 exhibits the lowest $1/\sigma_{ave}$ (0.898) and a dynamic yield stress comparable to that of PP0.3. Therefore, when disregarding the processing costs of RTPF, RTP0.6 can be considered as the optimal RTPF reinforced CTB mixture due to its lower cost, improved sustainability, and superior engineering performance compared to PP0.3. In other words, it is possible to replace PPF with twice the content of RTPF in CTB. Chen et al. have reached similar conclusions based on the flowability, static and dynamic mechanical properties of concrete (Chen et al., 2020a). But it should be noted that this section only briefly expounds the application potential of RTPF in CTB, and more evaluations need to be carried out for practical applications.

3.5. Performance optimization

The purpose of this section is to develop an easy-to-implement method to optimize the strength properties of RTPF reinforced CTB, especially the STS and FS. Based on previous studies (Li and Li, 2013; Meng and Khayat, 2017; Teng et al., 2020a), it can be clearly understood that the tensile/flexural properties of ultra-high-performance concrete (UHPC) and engineered cementitious composites (ECC) are closely related to the orientation and spatial dispersion of fibres in their matrices. And the viscosity of the matrix has been proven to have a significant impact on the orientation and dispersion of fibres (Sultangaliyeva et al., 2020). Inspired by this, improving the distribution of RTPF by controlling the rheology, especially the viscosity, of suspending CTB may be a promising approach to achieve the optimization of the tensile/flexural properties of RTPF reinforced CTB. To the best of the author's knowledge, studies on optimizing the performance of fibre reinforced CTB by controlling the rheology of suspending CTB are lacking so far. For the optimal RTPF content of 0.6 wt%, in this study, we attempted to determine the plastic viscosity corresponding to the optimal distribution of RTPF in CTB by manipulating the viscosity through thickeners. Prior to this, we aimed to establish a correlation between plastic viscosity and mini V-funnel flow rate to provide a simple alternative method for evaluating the plastic viscosity of suspending CTB.

Table 4
Inventory of cost, EC, and EE of all ingredients in CTB (M. Chen et al., 2021b; Du et al., 2022; Li et al., 2021; Norgate and Haque, 2010; Zhong and Zhang, 2021).

Ingredient	Cost (USD/kg)	EC (kg CO_2·eq/kg)	EE (MJ/kg)
Tailings	0	0.00747	0.153
Water	0.001	0	0.01
Cement	0.0687	0.912	5.5
PPF	9.8	2.7	100
RTPF	0.5	2.53	21.9

Fig. 14(a) shows the variations of the mini V-funnel flow rate and the equivalent plastic viscosity of CTB with thickener dosages. The increase in thickener dosage from 0 to 0.2 % results in a decrease in flow rate from 436.15 to 85.26 ml/s, and an increase in equivalent plastic viscosity from 0.693 to 3.756 Pa·s. The correlation between the equivalent plastic viscosity and the flow rate reveals a good linear relationship (Fig. 14(b)), indicating that the Marsh cone flow rate can serve as a reliable indirect indicator for on-site evaluation of CTB viscosity. Fig. 14 (c) plots the STS of RTPF reinforced CTB (0.6 wt% RTPF content) versus thickener dosage. It can be seen that when the thickener dosage is in the range of 0–0.1 %, the STS continues to increase while the standard error decreases. From a thickener dosage of 0.1–0.2 %, the STS starts to decrease while the standard error remains low. Therefore, the STS reaches its maximum (0.550 MPa) at a 0.1 % thickener dosage. This can be attributed to the optimal distribution of RTPF in suspending CTB at this time. While further increasing the thickener dosage, more air is entrapped and more voids are generated, resulting in a decrease in STS (Xue et al., 2019a). The above results indicate the existence of an optimal Marsh cone flow rate of approximately 133.41 ml/s (corresponding to a viscosity of 2.642 Pa·s), which ensures a good distribution of RTPF (0.6 wt%) without excessive air content. This Marsh cone flow rate can be used as a guideline for rheology control during RTPF reinforced CTB preparation to achieve a relatively uniform distribution of RTPF in the suspending CTB and thus optimize the tensile/flexural properties of RTPF reinforced CTB.

For the purpose of validating the rheology control method, a medium tailings (see Supplementary Data for details) was used to prepare suspending CTB with different thickener dosages (0, 0.025 %, 0.05 %, and 0.075 %). RTPF content is also fixed at 0.6 wt%. The corresponding flow rates are 354.38, 192.20, 138.29, and 118.13 ml/s, respectively. The splitting tensile test results are shown in Fig. 14(c). Among the four RTPF reinforced CTBs, when the thickener dosage is 0.05 %, the flow rate of the mixture is closest to the optimal flow rate (133.41 ml/s) and the highest STS (0.315 MPa) is obtained. Thus, this case study validated the effectiveness of the proposed rheology control approach to optimize the strength properties of RTPF reinforced CTB. It is important to note that the optimal thickener dosage varies depending on the mix composition of CTB. However, as long as the RTPF content is fixed, the optimal Marsh cone flow rate (or plastic viscosity) is a universal parameter.

4. Conclusion

This paper investigated the rheology (i.e., static yield stress, dynamic yield stress, and structural build-up), strength (i.e., uniaxial compressive, triaxial compressive, splitting tensile, and flexural strengths), microstructure, and life-cycle of CTB reinforced with different RTPF

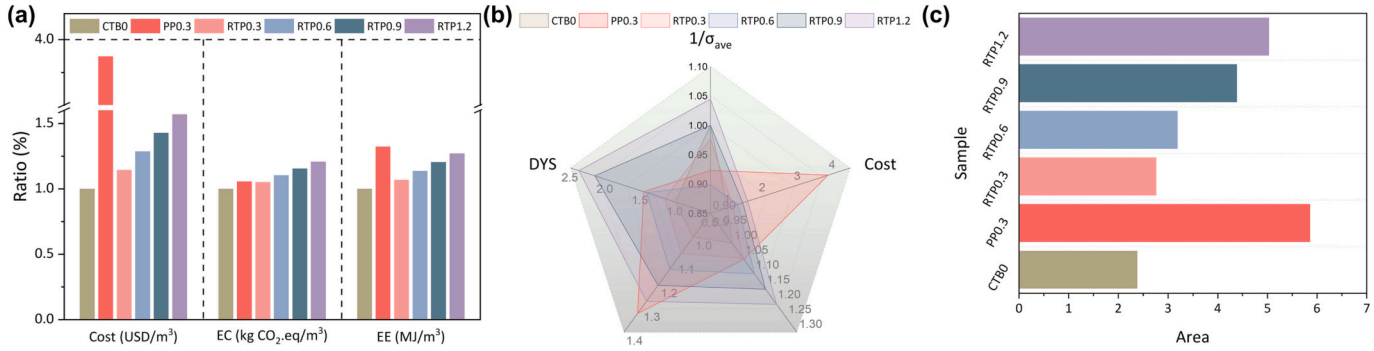

Fig. 13. (a) Cost, EC, and EE of all samples. (b) Economic, environmental and mechanical properties comparisons between all samples. (c) Summarized radar chart area of all samples. Note: DYS is the dynamic yield stress. σ_{ave} the ratio of the average value of UCS, STS and FS of RTPF reinforced CTB to the corresponding value of CTB0.

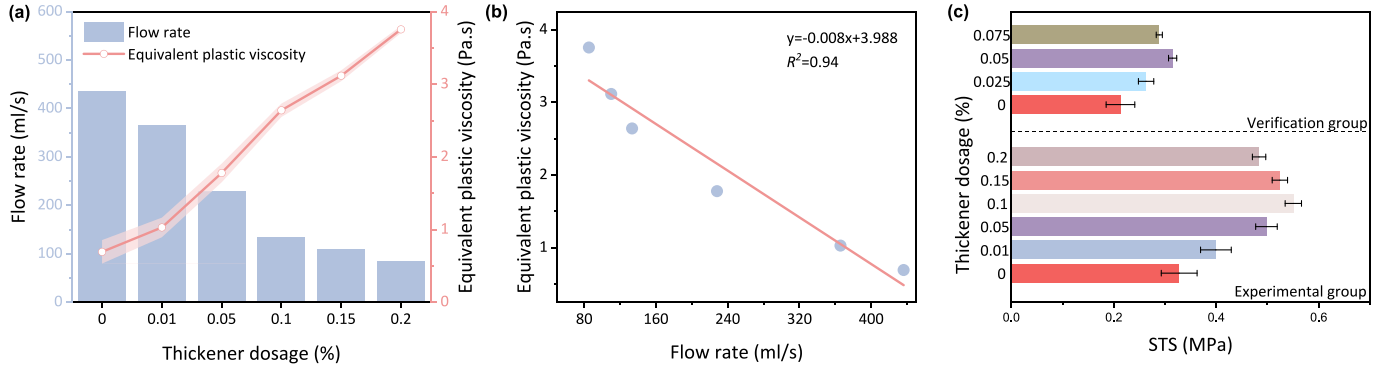

Fig. 14. Correlations between: (a) equivalent plastic viscosity, flow rate, and thickener dosage; (b) equivalent plastic viscosity and flow rate; (c) STS and thickener dosage.

contents (0.3, 0.6, 0.9, and 1.2 wt%). The mechanism behind the effect of RTPF on the dynamic yield stress of fresh CTB was revealed. The PPF reinforced CTB commonly used in mines was prepared, and its engineering performance was compared with RTPF reinforced CTB. A rheology control-based approach was proposed to enhance the strength performance of RTPF reinforced CTB. Based on these studies, the following main conclusions can be drawn:

- The dynamic yield stress and equivalent plastic viscosity of fresh CTB are improved by the inclusion of PPF and RTPF. The dynamic yield stress depends on the water film thickness and fibre flocculation effect, which can be well described by the mathematical model proposed herein. The RTP0.6 (CTB reinforced with 0.6 wt% RTPF) shows slightly better rheological properties compared with fresh PP0.3 (CTB reinforced with 0.3 wt% PPF).
- The PPF and RTPF have an insignificant effect on the cement hydration in fresh CTB, as they do not modify the distance between pseudo-contact regions. Consequently, the fresh CTB0, PP0.3 and RTP0.6 show comparable storage modulus evolutions. The PPF enhances the thixotropy of fresh CTB by improving flocculation, but such an enhancement is not observed in RTPF. As a result, the fresh PP0.3 exhibits first a nonlinear and then a linear increase in the evolution of the static yield stress, while the static yield stress of fresh RTP0.6 evolves linearly similar to that of the fresh CTB0. Compared with fresh CTB0 and PP0.3, the fresh RTP0.6 has the highest evolution rate of static yield stress due to the interpenetration and entanglement of RTPF in the fibre network.
- The mechanical properties (e.g., uniaxial compressive, triaxial compressive, splitting tensile, and flexural strengths) of hardened CTB increases first and then decreases with the increase of RTPF content. RTP0.6 has the best mechanical properties herein due to its superior pore size distribution and long-term hydration behaviour compared with samples RTP0.3, RTP0.9, RTP1.2 and PP0.3.
- The strength performance of RTPF reinforced CTB can be optimized by adjusting the viscosity of suspending CTB before the addition of RTPF. For a given RTPF content, the optimal viscosity may not be changed with the mix design of CTB. The viscosity can also be replaced by the easier obtained mini V-funnel flow rate to optimize the strength of RTPF reinforced CTB in practice.
- The comprehensive life cycle assessments from economic and environmental perspectives indicate that RTP0.6 is capable of reducing cost and improving sustainability compared with PP0.3. Remember that the RTP0.6 also shows comparable rheology and better mechanical properties compared with PP0.3. It means that the commonly used PPF in mines can be replaced with the RTPF with a twice content, achieving the local recovery of waste tyres.

This study focuses on the mechanical properties of RTPF reinforced CTB under static loadings. It is worth noting that the RTPF reinforced CTB also undergoes dynamic and time-dependent loadings in mining practices. The dynamic and time-dependent performances of RTPF reinforced CTB are an ongoing work. In addition, a more accurate cost evaluation for RTPF reinforced CTB is also imperative, encompassing separation expenses and related factors.

CRediT authorship contribution statement

Zhenbang Guo: Methodology, Validation, Formal analysis, Investigation, Writing - Original draft preparation. **Jingping Qiu**: Resources, Validation. **Alex Kirichek**: Validation, Formal analysis, Writing - Reviewing and Editing. **Hao Zhou** and **Chen Liu**: Validation, Investigation, Writing - Reviewing and Editing. **Lei Yang**: Conceptualization, Resources, Supervision, Writing - Reviewing and Editing.

Declaration of competing interest

The authors declare that they have no known competing financial interests or personal relationships that could have appeared to influence the work reported in this paper.

Data availability

Data will be made available on request.

Acknowledgments

Financial supports by Key Research and Development Project of Liaoning (2020JH1/10300005), National Key Research and Development Program (2019YFC1907202), and China Scholarship Council (No. 202206080032) are greatly appreciated. The authors also would like to thank Fan Yao from Shiyanjia Lab (www.shiyanjia.com) for technical support of rheological tests.

Appendix A. Supplementary data

Supplementary data to this article can be found online at https://doi.org/10.1016/j.scitotenv.2023.168320.

References

Ahrens, A., Bonde, A., Sun, H., Wittig, N.K., Hammershøj, H.C.D., Batista, G.M.F., Sommerfeldt, A., Frølich, S., Birkedal, H., Skrydstrup, T., 2023. Catalytic disconnection of C–O bonds in epoxy resins and composites. Nature 1–8.
Arunachalam, S.K., Muthiah, M., Rangaswamy, K.D., Kadarkarai, A., Arunasankar, C.G., 2021. Improving the structural performance of reinforced geopolymer concrete incorporated with hazardous heavy metal waste ash. World J. Eng. 19, 808–821.
Arunkumar, K., Muthiah, M., 2022. Invention of sustainable geopolymer concrete made with low calcium waste wood ash. World J. Eng. 19, 843–853.
Azevedo, F., Pacheco-Torgal, F., Jesus, C., De Aguiar, J.L.B., Camões, A.F., 2012. Properties and durability of HPC with tyre rubber wastes. Constr. Build. Mater. 34, 186–191.
Baricevic, A., Pezer, M., Rukavina, M.J., Serdar, M., Stirmer, N., 2018. Effect of polymer fibers recycled from waste tires on properties of wet-sprayed concrete. Constr. Build. Mater. 176, 135–144.
Baričević, A., Rukavina, M.J., Pezer, M., Štirmer, N., 2018. Influence of recycled tire polymer fibers on concrete properties. Cem. Concr. Compos. 91, 29–41.
Bennington, C.P.J., Kerekes, R.J., Grace, J.R., 1990. The yield stress of fibre suspensions. Can. J. Chem. Eng. 68, 748–757.
Cao, S., Yilmaz, E., Yin, Z., Xue, G., Song, W., Sun, L., 2021. CT scanning of internal crack mechanism and strength behavior of cement-fiber-tailings matrix composites. Cem. Concr. Compos. 116, 103865.
Chen, J.J., Ng, P.L., Kwan, A.K.H., Li, L.G., 2019. Lowering cement content in mortar by adding superfine zeolite as cement replacement and optimizing mixture proportions. J. Clean. Prod. 210, 66–76.
Chen, M., Zhong, H., Wang, H., Zhang, M., 2020a. Behaviour of recycled tyre polymer fibre reinforced concrete under dynamic splitting tension. Cem. Concr. Compos. 114, 103764.
Chen, M., Zhong, H., Zhang, M., 2020b. Flexural fatigue behaviour of recycled tyre polymer fibre reinforced concrete. Cem. Concr. Compos. 105, 103441.
Chen, M., Sun, Z., Tu, W., Yan, X., Zhang, M., 2021c. Behaviour of recycled tyre polymer fibre reinforced concrete at elevated temperatures. Cem. Concr. Compos. 124, 104257.
Chen, M., Zhong, H., Chen, L., Zhang, Y., Zhang, M., 2021d. Engineering properties and sustainability assessment of recycled fibre reinforced rubberised cementitious composite. J. Clean. Prod. 278, 123996.
Chen, Q., Zhang, Q., Fourie, A., Xin, C., 2017. Utilization of phosphogypsum and phosphate tailings for cemented paste backfill. J. Environ. Manag. 201, 19–27.
Chen, Q., Zhang, Q., Qi, C., Fourie, A., Xiao, C., 2018. Recycling phosphogypsum and construction demolition waste for cemented paste backfill and its environmental impact. J. Clean. Prod. 186, 418–429.
Chen, Q., Sun, S., Liu, Y., Qi, C., Zhou, H., Zhang, Q., 2021a. Immobilization and leaching characteristics of fluoride from phosphogypsum-based cemented paste backfill. Int. J. Miner. Metall. Mater. 28, 1440–1452.
Chen, Q., Tao, Y., Feng, Y., Zhang, Q., Liu, Y., 2021b. Utilization of modified copper slag activated by Na2SO4 and CaO for unclassified lead/zinc mine tailings based cemented paste backfill. J. Environ. Manag. 290, 112608.
Chen, Q., Tao, Y., Zhang, Q., Qi, C., 2022a. The rheological, mechanical and heavy metal leaching properties of cemented paste backfill under the influence of anionic polyacrylamide. Chemosphere 286, 131630.
Chen, Q., Zhu, L., Wang, Y., Chen, J., Qi, C., 2022b. The carbon uptake and mechanical property of cemented paste backfill carbonation curing for low concentration of CO2. Sci. Total Environ. 852, 158516.
Chen, Q., Zhou, H., Wang, Y., Wang, D., Zhang, Q., Liu, Y., 2023. Erosion wear at the bend of pipe during tailings slurry transportation: numerical study considering inlet velocity, particle size and bend angle. Int. J. Miner. Metall. Mater. 30, 1608–1620.
Cui, L., McAdie, A., 2023. Experimental study on evolutive fracture behavior and properties of sulfate-rich fiber-reinforced cemented paste backfill under pure mode-I, mode-II, and mode-III loadings. Int. J. Rock Mech. Min. Sci. 169, 105434.
Demirboğa, R., Türkmen, İbrahim, Karakoc, M.B., 2004. Relationship between ultrasonic velocity and compressive strength for high-volume mineral-admixtured concrete. Cem. Concr. Res. 34, 2329–2336.
Dobrotă, D., Dobrotă, G., Dobrescu, T., 2020. Improvement of waste tyre recycling technology based on a new Tyre markings. J. Clean. Prod. 260, 121141.
Douara, T.H., Guettala, S., Hadji, T., Attia, A., 2022. Strength assessment and durability of self-compacting concrete manufactured with various fine aggregates subjected to acidic curing environment. World J. Eng. 19, 570–582.
Du, J., Liu, Z., Christodoulatos, C., Conway, M., Bao, Y., Meng, W., 2022. Utilization of off-specification fly ash in preparing ultra-high-performance concrete (UHPC): mixture design, characterization, and life-cycle assessment. Resour. Conserv. Recycl. 180, 106136.
Fall, M., Belem, T., Samb, S., Benzaazoua, M., 2007. Experimental characterization of the stress-strain behaviour of cemented paste backfill in compression. J. Mater. Sci. 42, 3914–3922.
Fall, M., Benzaazoua, M., Saa, E.G., 2008. Mix proportioning of underground cemented tailings backfill. Tunn. Undergr. Space Technol. 23, 80–90.
Fall, M., Célestin, J.C., Pokharel, M., Touré, M., 2010. A contribution to understanding the effects of curing temperature on the mechanical properties of mine cemented tailings backfill. Eng. Geol. 114, 397–413.
Fung, W.W.S., Kwan, A.K.H., 2010. Role of water film thickness in rheology of CSF mortar. Cem. Concr. Compos. 32, 255–264.
Ghirian, A., Fall, M., 2013. Coupled thermo-hydro-mechanical–chemical behaviour of cemented paste backfill in column experiments. Part I: physical, hydraulic and thermal processes and characteristics. Eng. Geol. 164, 195–207.
Guo, Z., Qiu, J., Jiang, H., Xing, J., Sun, X., Ma, Z., 2021. Flowability of ultrafine-tailings cemented paste backfill incorporating superplasticizer: insight from water film thickness theory. Powder Technol. 381, 509–517.
Guo, Z., Qiu, J., Pel, L., Zhao, Y., Zhu, Q., Kwek, J.W., Zhang, L., Jiang, H., Yang, J., Qu, Z., 2023. A contribution to understanding the rheological measurement, yielding mechanism and structural evolution of fresh cemented paste backfill. Cem. Concr. Compos. 143, 105221.
Hong, Z., Tao, M., Cui, X., Wu, C., Zhao, M., 2023. Experimental and numerical studies of the blast-induced overbreak and underbreak in underground roadways. Undergr. Space 8, 61–79.
Islam, M.M.U., Li, J., Roychand, R., Saberian, M., Chen, F., 2022. A comprehensive review on the application of renewable waste tire rubbers and fibers in sustainable concrete. J. Clean. Prod. 133998.
Jiang, G., Wu, A., Wang, Y., Li, J., 2019. The rheological behavior of paste prepared from hemihydrate phosphogypsum and tailing. Constr. Build. Mater. 229, 116870.
Jin, S., Zhang, J., Han, S., 2017. Fractal analysis of relation between strength and pore structure of hardened mortar. Constr. Build. Mater. 135, 1–7.
Kanta, N.R., Ponnada, M.R., 2022. Performance of spent garnet sand and used foundry sand as fine aggregate in concrete. World J. Eng. 19, 632–638.
Khial, N., Chaid, R., 2022. Assessment of the aggressive agents' penetration into concrete by non-destructive techniques. World J. Eng. 19, 735–742.
Koohestani, B., Belem, T., Koubaa, A., Bussière, B., 2016. Experimental investigation into the compressive strength development of cemented paste backfill containing nano-silica. Cem. Concr. Compos. 72, 180–189.
Kwan, A.K.H., Fung, W.W.S., 2009. Packing density measurement and modelling of fine aggregate and mortar. Cem. Concr. Compos. 31, 349–357.
Kwan, A.K.H., Fung, W.W.S., 2012. Roles of water film thickness and SP dosage in rheology and cohesiveness of mortar. Cem. Concr. Compos. 34, 121–130.
Kwan, A.K.H., Chan, K.W., Wong, V., 2013. A 3-parameter particle packing model incorporating the wedging effect. Powder Technol. 237, 172–179.
Lecompte, T., Perrot, A., 2017. Non-linear modeling of yield stress increase due to SCC structural build-up at rest. Cem. Concr. Res. 92, 92–97.
Li, C., Zhang, N., Zhang, J., Song, S., Zhang, Y., 2021. CASH gel and pore structure characteristics of alkali-activated red mud–iron tailings cementitious mortar. Materials (Basel) 15, 112.
Li, L.G., Kwan, A.K.H., 2013. Concrete mix design based on water film thickness and paste film thickness. Cem. Concr. Compos. 39, 33–42.
Li, L.G., Zhuo, H.X., Zhu, J., Kwan, A.K.H., 2019. Packing density of mortar containing polypropylene, carbon or basalt fibres under dry and wet conditions. Powder Technol. 342, 433–440.
Li, M., Li, V.C., 2013. Rheology, fiber dispersion, and robust properties of engineered cementitious composites. Mater. Struct. Constr. 46, 405–420.
Libos, I.L.S., Cui, L., Liu, X., 2021. Effect of curing temperature on time-dependent shear behavior and properties of polypropylene fiber-reinforced cemented paste backfill. Constr. Build. Mater. 311, 125302.
Lowke, D., 2018. Thixotropy of SCC—a model describing the effect of particle packing and superplasticizer adsorption on thixotropic structural build-up of the mortar phase based on interparticle interactions. Cem. Concr. Res. 104, 94–104.
Luo, X., Gao, J., Li, S., Xu, Z., Chen, G., 2022. Experimental study on the early-age properties of cement pastes with recycled brick powder. Constr. Build. Mater. 347, 128584.
Ma, S., Qian, Y., Kawashima, S., 2018. Experimental and modeling study on the non-linear structural build-up of fresh cement pastes incorporating viscosity modifying admixtures. Cem. Concr. Res. 108, 1–9.

Meng, W., Khayat, K.H., 2017. Improving flexural performance of ultra-high-performance concrete by rheology control of suspending mortar. Compos. Part B Eng. 117, 26–34.
Merli, R., Preziosi, M., Acampora, A., Lucchetti, M.C., Petrucci, E., 2020. Recycled fibers in reinforced concrete: a systematic literature review. J. Clean. Prod. 248, 119207.
Mohajerani, A., Burnett, L., Smith, J.V., Markovski, S., Rodwell, G., Rahman, M.T., Kurmus, H., Mirzababaei, M., Arulrajah, A., Horpibulsuk, S., et al., 2020. Recycling waste rubber tyres in construction materials and associated environmental considerations: a review. Resour. Conserv. Recycl. 155, 104679.
Mucsi, G., Szenczi, Á., Nagy, S., 2018. Fiber reinforced geopolymer from synergetic utilization of fly ash and waste tire. J. Clean. Prod. 178, 429–440.
Norgate, T., Haque, N., 2010. Energy and greenhouse gas impacts of mining and mineral processing operations. J. Clean. Prod. 18, 266–274.
Onuaguluchi, O., Banthia, N., 2017. Durability performance of polymeric scrap tire fibers and its reinforced cement mortar. Mater. Struct. 50, 1–10.
Onuaguluchi, O., Banthia, N., 2019. Value-added reuse of scrap tire polymeric fibers in cement-based structural applications. J. Clean. Prod. 231, 543–555.
Perrot, A., Lecompte, T., Estellé, P., Amziane, S., 2013. Structural build-up of rigid fiber reinforced cement-based materials. Mater. Struct. 46, 1561–1568.
Qi, C., Fourie, A., 2019. Cemented paste backfill for mineral tailings management: review and future perspectives. Miner. Eng. 144, 106025.
Qi, C., Fourie, A., Chen, Q., 2018a. Neural network and particle swarm optimization for predicting the unconfined compressive strength of cemented paste backfill. Constr. Build. Mater. 159, 473–478.
Qi, C., Fourie, A., Chen, Q., Zhang, Q., 2018b. A strength prediction model using artificial intelligence for recycling waste tailings as cemented paste backfill. J. Clean. Prod. 183, 566–578.
Qiu, J., Guo, Z., Yang, L., Jiang, H., Zhao, Y., 2020. Effects of packing density and water film thickness on the fluidity behaviour of cemented paste backfill. Powder Technol. 359, 27–35.
Qu, Z., Yu, Q., Ong, G.P., Cardinaels, R., Ke, L., Long, Y., Geng, G., 2023. 3D printing concrete containing thermal responsive gelatin: towards cold environment applications. Cem. Concr. Compos. 140, 105029.
Roshani, A., Fall, M., 2020. Rheological properties of cemented paste backfill with nano-silica: link to curing temperature. Cem. Concr. Compos. 114, 103785.
Roussel, N., Ovarlez, G., Garrault, S., Brumaud, C., 2012. The origins of thixotropy of fresh cement pastes. Cem. Concr. Res. 42, 148–157.
Ruan, S., Liu, L., Zhu, M., Shao, C., Xie, L., Hou, D., 2023. Application of desulfurization gypsum as activator for modified magnesium slag-fly ash cemented paste backfill material. Sci. Total Environ. 869, 161631.
Serdar, M., Baričević, A., Jelčić Rukavina, M., Pezer, M., Bjegović, D., Štirmer, N., 2015. Shrinkage behaviour of fibre reinforced concrete with recycled tyre polymer fibres. Int. J. Polym. Sci. 2015.
Siddika, A., Al Mamun, M.A., Alyousef, R., Amran, Y.H.M., Aslani, F., Alabduljabbar, H., 2019. Properties and utilizations of waste tire rubber in concrete: a review. Constr. Build. Mater. 224, 711–731.
Song, X., Zhang, J., Shang, S., 2017. Mechanical properties of early-age concrete reinforced with multi-walled carbon nanotubes. Mag. Concr. Res. 69, 683–693.
Sultangaliyeva, F., Carré, H., La Borderie, C., Zuo, W., Keita, E., Roussel, N., 2020. Influence of flexible fibers on the yield stress of fresh cement pastes and mortars. Cem. Concr. Res. 138, 106221.
Teng, L., Meng, W., Khayat, K.H., 2020a. Rheology control of ultra-high-performance concrete made with different fiber contents. Cem. Concr. Res. 138, 106222.
Teng, L., Zhu, J., Khayat, K.H., Liu, J., 2020b. Effect of welan gum and nanoclay on thixotropy of UHPC. Cem. Concr. Res. 138, 106238.
Thomas, B.S., Gupta, R.C., 2016. A comprehensive review on the applications of waste tire rubber in cement concrete. Renew. Sust. Energ. Rev. 54, 1323–1333.
Xin, J., Liu, L., Xu, L., Wang, J., Yang, P., Qu, H., 2022. A preliminary study of aeolian sand-cement-modified gasification slag-paste backfill: fluidity, microstructure, and leaching risks. Sci. Total Environ. 830, 154766.
Xu, W., Li, Q., Liu, B., 2020a. Coupled effect of curing temperature and age on compressive behavior, microstructure and ultrasonic properties of cemented tailings backfill. Constr. Build. Mater. 237, 117738.
Xu, W., Zhang, Y., Zuo, X., Hong, M., 2020b. Time-dependent rheological and mechanical properties of silica fume modified cemented tailings backfill in low temperature environment. Cem. Concr. Compos. 114, 103804.
Xu, Y., Xing, G., Zhao, J., Zhang, Y., 2021. The effect of polypropylene fiber with different length and dosage on the performance of alkali-activated slag mortar. Constr. Build. Mater. 307, 124978.
Xue, G., Yilmaz, E., 2022. Strength, acoustic, and fractal behavior of fiber reinforced cemented tailings backfill subjected to triaxial compression loads. Constr. Build. Mater. 338, 127667.
Xue, G., Yilmaz, E., Song, W., Cao, S., 2019a. Mechanical, flexural and microstructural properties of cement-tailings matrix composites: effects of fiber type and dosage. Compos. Part B Eng. 172, 131–142.
Xue, G., Yilmaz, E., Song, W., Cao, S., 2019b. Analysis of internal structure behavior of fiber reinforced cement-tailings matrix composites through X-ray computed tomography. Compos. Part B Eng. 175, 107091.
Yan, R., Liu, J., Yin, S., Zou, L., Kou, Y., Zhang, P., 2022. Effect of polypropylene fiber and coarse aggregate on the ductility and fluidity of cemented tailings backfill. J. Cent. South Univ. 29, 515–527.
Yang, L., Xu, W., Yilmaz, E., Wang, Q., Qiu, J., 2020. A combined experimental and numerical study on the triaxial and dynamic compression behavior of cemented tailings backfill. Eng. Struct. 219, 110957.
Yi, X.W., Ma, G.W., Fourie, A., 2015. Compressive behaviour of fibre-reinforced cemented paste backfill. Geotext. Geomembr. 43, 207–215.
Yin, S., Shao, Y., Wu, A., Wang, H., Liu, X., Wang, Y., 2020. A systematic review of paste technology in metal mines for cleaner production in China. J. Clean. Prod. 247, 119590.
Yin, S., Chen, W., Wang, Y., 2021a. Effect of mixed bacteria on cemented tailings backfill: economic potential to reduce binder consumption. J. Hazard. Mater. 411, 125114.
Yin, S., Hou, Y., Chen, X., Zhang, M., 2021b. Mechanical, flowing and microstructural properties of cemented sulfur tailings backfill: effects of fiber lengths and dosage. Constr. Build. Mater. 309, 125058.
Yu, Z., Wang, Y., Li, J., 2022. Performance investigation and cost–benefit analysis of recycled tire polymer fiber-reinforced cemented paste backfill. Polymers (Basel) 14, 708.
Zhang, J., Ye, H., Gao, X., Wu, W., 2022. Adsorption and desorption of polycarboxylate ether superplasticizer in fresh cementitious materials blended with mineral admixtures. J. Mater. Res. Technol. 17, 1740–1751.
Zhang, S., Yang, L., Ren, F., Qiu, J., Ding, H., 2020. Rheological and mechanical properties of cemented foam backfill: effect of mineral admixture type and dosage. Cem. Concr. Compos. 112, 103689.
Zhong, H., Zhang, M., 2020. Experimental study on engineering properties of concrete reinforced with hybrid recycled tyre steel and polypropylene fibres. J. Clean. Prod. 259, 120914.
Zhong, H., Zhang, M., 2021. Effect of recycled tyre polymer fibre on engineering properties of sustainable strain hardening geopolymer composites. Cem. Concr. Compos. 122, 104167.
Zhong, H., Zhang, M., 2022a. Effect of recycled polymer fibre on dynamic compressive behaviour of engineered geopolymer composites. Ceram. Int. 48, 23713–23730.
Zhong, H., Zhang, M., 2022b. Dynamic splitting tensile behaviour of engineered geopolymer composites with hybrid polyvinyl alcohol and recycled tyre polymer fibres. J. Clean. Prod. 379, 134779.